Laboratory insights into the effect of sediment-hosted methane hydrate morphology on elastic wave velocity from time-lapse 4D synchrotron X-ray computed tomography.

Sourav K. Sahoo[1,2], Madhusudhan B.N[3], Hector Marín-Moreno[1], Laurence J. North[1], Sharif Ahmed[3], Ismael Himar Falcon-Suarez[1], Tim A. Minshull[2] and Angus I. Best[1]

[1]*National Oceanography Centre, University of Southampton Waterfront Campus, European Way, Southampton, SO14 3ZH, United Kingdom.*

[2]*National Oceanography Centre Southampton, University of Southampton, European Way, Southampton, SO14 3ZH, United Kingdom.*

[3]*Faculty of Engineering and the Environment, University of Southampton, Southampton, United Kingdom*

Corresponding author: Sourav K. Sahoo (s.sahoo@noc.ac.uk)

Key Points

We observe the evolution of methane hydrate morphology in porous media by 4D X-ray CT imaging and laboratory geophysical experiments.

X-ray CT shows that hydrate morphology evolves from an initial pore-floating, to pore-bridging, to a final inter-pore hydrate framework.

We found anomalously low S-wave velocity probably caused by the presence of water films between hydrate and host grains.

Abstract

A better understanding of the effect of methane hydrate morphology and saturation on elastic wave velocity of hydrate bearing sediments is needed for improved seafloor hydrate resource and geohazard assessment. We conducted X-ray synchrotron time-lapse 4D imaging of methane hydrate evolution in Leighton Buzzard sand, and compared the results to analogous hydrate formation and dissociation experiments in Berea sandstone, on which we measured ultrasonic P- and S-wave velocity, and electrical resistivity. The imaging experiment showed that initially hydrate envelops gas bubbles and methane escapes from these bubbles via rupture of hydrate shells, leading to smaller bubbles. This process leads to a transition from pore-floating to pore-bridging hydrate morphology. Finally, pore-bridging hydrate coalesces with that from adjacent pores creating an inter-pore hydrate framework that interlocks the sand grains. We also observed isolated pockets of gas within hydrate. We observed distinct changes in gradient of P- and S-wave velocity increase with hydrate saturation. Informed by a theoretical model of idealized hydrate morphology and its influence on elastic wave velocity, we were able to link velocity changes to hydrate morphology progression from initial pore-floating, then pore-bridging, to an inter-pore hydrate framework. The latter observation is the first evidence of this type of hydrate morphology, and its measurable effect on velocity. We found anomalously low S-wave velocity compared to the effective medium model, probably caused by the presence of a water film between hydrate and mineral grains.

1 Introduction

Gas hydrates are naturally occurring ice-like clathrate compounds that form when sufficient gas (methane is the most common in nature) and water coexist under low temperatures and high pressures, generally found in marine and permafrost environments (Kvenvolden, 1993). Currently, seafloor gas hydrates are being considered as a viable alternative energy resource (Boswell & Collett, 2011), and may have an important role in future climate change (Archer et al., 2009), carbon dioxide sequestration (Jung et al., 2010) and continental slope stability (Sultan et al., 2004). As such, it is important to obtain accurate estimates of the amount and distribution of gas hydrates, largely reliant on geophysical remote sensing technologies and data interpretation. Such estimates depend on knowledge of hydrate formation processes and how they affect geophysical properties. In general, the presence of hydrate increases the seismic velocity (Helgerud et al., 1999) and electrical resistivity (Edwards, 1997) of host sediments; this depends on the amount of hydrate occupying the pore space (saturation) and hydrate morphology, i.e., spatial distribution of the hydrate grains within the host sediment (e.g., Dai et al., 2012; Ecker et al., 2000; Priest et al., 2005; Waite et al., 2009). In particular, geophysical remote sensing methods use elastic wave velocity and electrical resistivity anomalies to quantify hydrates in marine sediments, based on rock physics models that relate these anomalies to hydrate content (e.g., Collett, 2001; Cook & Waite, 2018; Doveton, 2001; Ecker et al., 2000; Edwards, 1997; Helgerud et al., 1999; Spangenberg, 2001).

Accurate quantification of *in situ* methane hydrates is hampered by our limited understanding of the effects of hydrate content, morphology and distribution on the geophysical properties of the hydrate bearing sediments, along with sediment type, porosity, permeability, and pore fluid salinity (e.g., Waite et al., 2009). These effects are difficult to understand unambiguously from studies of natural samples alone because of spatial averaging. Moreover, using natural samples for laboratory studies of geophysical and geomechanical properties is challenging because: (i) coring is technically difficult and requires expensive drill ships with pressurised sampling capability; and (ii) absolute preservation of *in situ* conditions is not possible currently (Tulk, 1999). However, controlled laboratory experiments on synthetic hydrate samples offer a viable alternative to gain insights into the physical properties of hydrate-bearing sediments. Synthetic hydrate samples allow exploration of potentially the full range of hydrate saturations and

morphologies for different sediment types, although laboratory methods have their own challenges.

Notable insights have been gained from laboratory studies to date (e.g., Handa, 1990; Kerkar et al., 2014; Priegnitz et al., 2015; Priest et al., 2009; Tohidi et al., 2001), but further research is needed into the following areas: i) the causes of the commonly observed discrepancy between hydrate saturation estimates from seismo-acoustic and electrical resistivity methods (Attias et al., 2016; Goswami et al., 2015; Lee & Collett, 2006; Miyakawa et al., 2014; Sahoo et al., 2018) (referred to here as the seismic-electrical discrepancy); and ii) the effect of methane hydrate saturation and its spatial distribution in the host sediment on the seismo-acoustic velocity of hydrate bearing sediments. Some studies associate the seismic-electrical discrepancy to the coexistence of gas and hydrate, as the presence of gas can reduce the seismic velocity but not the electrical resistivity of the sediment (e.g., Goswami et al., 2015; Lee & Collett, 2006; Miyakawa et al., 2014; Sahoo et al., 2018). This discrepancy could also be due to incorrect assumptions about the morphology or distribution of hydrate within the pores.

Natural hydrates commonly exist in several different morphologies (or habits) within the host sediments. In this study, the term “morphology” refers to the spatial distribution of the hydrate grains within the host sediment. Natural hydrate can be broadly divided into two main types based on its morphology : sediment grain displacing or pore-fluid displacing hydrate (e.g., Holland et al., 2008). Sediment grain displacing hydrate physically moves apart sediment grains, forming solid hydrate volumes larger than the original sediment pore size; examples include hydrate veins, layers, and lenses generally found in fine-grained sediments (e.g., Holland et al., 2008). By contrast, pore fluid displacing hydrate grows inside the intact structure of sediment pores. Most pore fluid displacing natural hydrate is observed in cores from coarse-grained silty or sandy layers. For example, cores from NGHP1 (Collett et al., 2015) and IODP Expedition 311 (Riedel et al., 2010) showed pore fluid displacing hydrate in coarse-grained layers. Such sandy units are often the targets for hydrate reservoirs of potential economic importance, and we restrict this study to pore-fluid displacing hydrate.

Pore-fluid displacing hydrate can be sub-divided into cementing or non-cementing morphologies (Figure 1) based on whether hydrate grows adhering to sediment grains or floating in the pore fluid inside the pore space (e.g. Ecker et al., 1998). The distinction between different pore-fluid displacing hydrate morphologies were initially deduced from the effect of hydrate morphology on elastic wave velocity (e.g. Ecker et al., 1998). . Cementing morphology occurs when hydrate bonds the host mineral grain contacts (Ecker et al., 1998); the effect on elastic wave velocity was conceptualized as either hydrate located exclusively at grain contacts (contact cementing) or hydrate evenly coating mineral grains (grain coating), a proportion of which bonds grain contacts (Ecker et al., 1998; Helgerud et al., 1999). Several studies (e.g., Chand et al., 2006; Priest et al., 2005) have deduced from elastic wave measurements that hydrate forms cement under excess gas conditions by coating the mineral grains, with a fraction of the hydrate saturation acting as cement. Formation of hydrate in cementing or non-cementing morphology also depends on the sediment mineralogy; clay and sand interact with hydrate differently (Kumar et al., 2015; Sloan & Koh, 2007). By contrast, non-cementing hydrate forms when hydrate grows away from the sediment grain contacts (Ecker et al., 1998). The cementing morphology has a much greater effect on the elastic properties of hydrate-bearing sediments than the non-cementing morphology (e.g., Best et al., 2013; Ecker et al., 1998; Priest et al., 2009; Waite et al., 2004). However, the non-cementing morphology is thought to dominate natural hydrate systems, and has been sampled, or inferred, at locations such as Mallik, Mackenzie Delta (Uchida et al., 2000), the Nankai Trough (e.g. Fujii et al., 2015), Alaminos Canyon, Gulf of Mexico (Boswell et al., 2009), and Mount Elbert, Alaska North Slope (Stern et al., 2011). Useful summaries of observations of hydrate morphologies at various sites around the world are given in Holland et al. (2008) and in Dai et al. (2012).

If non-cementing hydrate grows in the pore space without bridging neighbouring sediment grains, then it is termed pore-floating (Hu et al., 2014) or pore-filling hydrate (i.e. hydrate may be partially filling the pore, but not contacting more than one grain of the sand frame). In this manuscript, we use the term “pore-floating” for such a hydrate morphology. If hydrate bridges neighbouring sediment grains (i.e. contacts more than one grain in the sand frame) then this is termed “frame-supporting” or “load-bearing” or “pore-bridging” hydrate. We will use the term “pore-bridging” to describe this morphology, which has been reported for pore-floating hydrate

saturations greater than 25 - 40% (Hu et al., 2014; Priest et al., 2009; Waite et al., 2009). Priest et al. (2009) deduced a pore-bridging morphology for methane hydrate formed in sand under excess water conditions from observed increases in seismic velocity at hydrate saturations higher than 30%; for saturations of 10% and 15%, the seismic velocity was between those for pore-bridging and pore-floating hydrate (Priest et al., 2009). (Yun et al., 2005) showed that Tetrahydrofuran (THF) hydrate grows in the pore-floating morphology up to 40% hydrate saturation; for higher saturations, the measured velocity was much higher than that predicted for the pore-floating morphology, qualitatively consistent with a pore-bridging morphology. While cementing and pore-bridging hydrate are both associated with an increase in the elastic moduli of the composite sediment, pore-floating hydrate affects the elastic properties of the pore-fluid (e.g., Ecker et al., 2000).

Studies of gas hydrate using techniques like X-ray imaging have shown that gas hydrate often has a complex morphology. Recent studies in sands suggest that a thin film of water is present between the host mineral grains and the hydrate (Bonnefoy et al., 2005; Chaouachi et al., 2015; Sell et al., 2018; Tohidi et al., 2001). This water film should exist for both cementing and pore-bridging hydrate in sands.

Recently, Sahoo et al. (2018) found hydrate formation does not take up all the methane gas or water even if the system is under two phase water-hydrate stability conditions, leading to coexisting gas, water and hydrate. Sahoo et al., (2018) deduced this coexistence of gas and hydrate using thermodynamic calculations from pore pressure and temperature measurements. The authors hypothesised that the dominant mechanism for coexisting gas is the formation of hydrate films around methane gas bubbles. Also, co-existence of gas and hydrate in the gas hydrate stability zone (GHSZ) has been inferred in natural sediments (e.g., Guerin et al., 1999; Milkov et al., 2004; Lee and Collett, 2006; Miyakawa et al., 2014). Researchers have attributed this coexistence to the following causes: (i) influx of gas into the GHSZ along fractures or faults (Gorman et al., 2002; Lee & Collett, 2006; Smith et al., 2014); (ii) local deviations from two phase water-hydrate stability conditions (pressure-temperature-salinity) resulting in local hydrate dissociation within the GHSZ (Guerin et al., 1999; Milkov et al., 2004); or (iii) hydrate formation kinetics (Torres et al., 2004). Inclusions of gas within hydrate can also enable coexistence of gas with hydrate in two phase water-hydrate stability conditions (e.g., Schicks et

al., 2006). Hydrate formation on the surface of gas bubbles results in isolation of the remaining gas inside the hydrate shell from the pore water outside, leading to co-existing gas. Sahoo et al., (2018) showed experimentally that coexisting gas can cause significant errors in hydrate saturation calculations from electrical resistivity, as both hydrate and gas are resistive compared to seawater. Coexistence of gas and hydrate can also cause uncertainty in local hydrate saturation estimation from electrical resistivity. For example, Miyakawa et al., (2014) proposed that co-existing gas and hydrate leads to a velocity decrease with no corresponding decrease in resistivity in the Kumano basin, Nankai, Japan. Other such discrepancies found in the literature are listed in Table 1 of Sahoo et al. (2018).

In this study, we set out to observe changes in geophysical properties during methane hydrate growth in coarse-grained hydrate reservoir analogues (porous media), and to link them to observed changes in hydrate morphology using time-lapse (4D) X-ray CT imaging of the pore spaces. We also want to image the mechanism of co-existing gas and hydrate in two-phase water-hydrate stability condition. To achieve this, we conducted two separate laboratory hydrate formation and dissociation experiments, one on Berea sandstone to obtain ultrasonic P- and S-wave velocity and electrical resistivity variations with hydrate saturation, and another on Leighton Buzzard sand to obtain 4D time-lapse images from synchrotron radiation X-ray computed tomography (SR-XCT). We then used the effective medium rock physics model of Marín-Moreno et al. (2017) to predict the effect of changing hydrate morphology on elastic wave velocities based on previously conceived idealised hydrate morphologies (pore-floating and pore-bridging). The X-ray imaging confirmed the existence of these idealised morphologies at certain periods during hydrate formation, and provided the first known direct evidence for a third morphology, here called inter-pore hydrate framework. This last morphology was inferred to affect the elastic velocities, although not modelled. Also, lower than expected S-wave velocities were attributed to the presence of a water film between the inter-pore hydrate framework and the host porous medium..

Overall, our results provide further evidence of how methane hydrate saturation relates to hydrate morphology, of how this morphology influences elastic wave velocity and electrical resistivity, two important geophysical parameters used in hydrate exploration, and of the mechanism of coexisting gas and hydrate.

2 Methods

2.1 Porous media

We used a cylindrical sample (4.97 cm diameter and 2.06 cm height) of Berea sandstone with a porosity of 0.22, permeability of 448 mD (4.48×10^{-13} m^2) as a stable, inert, and well-characterized porous medium for the ultrasonic experiment. The use of loose sand would have been preferable as a seafloor hydrate analogue, but the available pulse-echo system was configured for rock samples only. The grain size is about 100 μm, similar to observations by other researchers (e.g., Minagawa et al., 2008). X-ray diffraction analysis of the sample Berea rock by Han et al. (2015) showed 1.7% illite and 3.3% K feldspar in volume. For the synchrotron imaging experiment, we weighed and tamped Leighton Buzzard sand (a mean grain size d_{50} =100 μm) directly into the cylindrical hydrate rig (2 mm diameter and 23 mm height) to obtain a sample of 35% porosity (a typical permeability is several Darcies for such sand packs). We tried to cut a 2 mm diameter Berea sandstone sample suitable for synchrotron imaging, but the Berea disintegrated during the attempts. Lee, (2008) found that the permeability of gas hydrate bearing sediment at the Mallik 5L-38 with hydrate saturation between 12% and 34% to be very similar to the permeability of hydrate bearing Berea sandstone (Kleinberg et al., 2003), and maximum hydrate saturation in our experiment was 26%. Therefore, we choose Leighton Buzzard sand for the synchrotron experiments, which has a similar quartz mineralogy (although uncemented). We used the same hydrate formation method in both experiments according to Section 2.2 (i.e hydrate forming from gas bubbles, in an excess water environment, with a water wet sediment). Given the similar mineralogies and grain shapes of the host porous samples, we assume there is no significant difference in hydrate morphology evolution between experiments, although this has not been verified. Each sample was firstly oven-dried at 60 ˚C before placing in their respective experimental rigs.

2.2 Hydrate formation

We followed the method of Sahoo et al. (2018) and Waite et al. (2004) with high initial brine saturation (83.5% for ultrasonic and 90% for synchrotron samples, respectively) giving excess water conditions (Ellis, 2008; Priest et al., 2009). Our experimental setup with gas injected from the base of the sample represents gas hydrate systems with localized gas flow, such as at the base of the gas hydrate stability zone (GHSZ), or near to gas chimneys.

An initial hydrostatic triaxial confining pressure of 10 MPa was applied to the Berea sample in the ultrasonic rig to ensure the integrity of coupling between the sample and buffer rods (confining pressure was provided by the reaction of the rigid sample container to applied pore pressure in the synchrotron sample). A pore fluid line vacuum (<1 Pa) was applied to each sample to maximize the removed air from the pore space. Still under vacuum, 3.5 wt% NaCl deionized and deaerated water solution was injected to partially fill the sample pore spaces (83.5% for ultrasonic and 90% synchrotron samples). The partially saturated samples were left under vacuum conditions for 3 days, to favor a homogeneous pore fluid distribution throughout the sample by capillary forces. The brine imbibition and distribution was facilitated by brine injection after an applied vacuum, and by the high wettability of the quartz grains. Thus, we assume water vapor and any remaining air occupied the remaining pore space of each sample.

In the ultrasonic experiments, methane gas was injected to achieve a pore fluid pressure of 11.9 MPa and, and the confining pressure was increased simultaneously to 21.9 MPa to maintain a constant differential pressure of 10 MPa (confining minus pore pressure). The pore fluid system was then sealed, keeping the pore fluid line between the sample and valve V_A (Figure 2a) filled with methane gas, which is free to move in and out of the sample as a result of potential pore pressure variations Buoyancy could make the gas to accumulate in the upper part of the sample. However, that was not the case in our experiment, as we did not identify internal reflections in the P-wave signal (in addition to the top and base sample reflections; Supplementary Figure S1). The initial gas and water distribution in the synchrotron rig was observed from the 3D imaging, discussed in Section 3.1. Finally, hydrate was formed by cooling each system to fall within the

gas hydrate stability conditions (Figure 3) and above the freezing point of water. After hydrate formation, dissociation was achieved by heating the system (Figure 3).

The hydrate formation procedure was similar in both experiments with slight variations as described below. Ultrasonic P- and S-wave velocities of Berea sandstone are known to be sensitive to changes in differential pressure due to microcracks in mineral grains (e.g., Nur & Simmons, 1969). Hence, a constant differential pressure was maintained in the ultrasonic rig to rule out any such effects. This approach ensured that any change in velocity could be attributed to changes in pore fluids and hydrate formation only. Four cycles of hydrate formation and dissociation were completed in the ultrasonic rig; a differential pressure of 10 MPa was maintained for cycles 1 and 2, and 55 MPa for cycles 3 and 4. Hydrate, gas and brine saturation were calculated from the measured pressure and temperature changes of the system using a thermodynamic method (Sahoo et al., 2018). In the synchrotron rig, no confining pressure was applied, with a pressure cell (made from PEEK) providing rigid confinement. We applied 10 MPa of methane pressure directly through the injection inlet, filling the pore fluid pipe and sand sample volume with a pre-calculated amount of brine solution. We then left the rig for three days for the pore fluids to redistribute within the pore space. Only one cycle of hydrate formation and dissociation was performed in the synchrotron rig.

2.3 Ultrasonic velocity and electrical resistivity measurements

We used a stainless steel high-pressure cell, designed to host 5 cm diameter rock samples under hydrostatic confining pressure up to 65 MPa (Figure 2a) (Ellis, 2008). The cell was instrumented to monitor pore fluid pressure, and the inner and outer (ambient) cell temperature. The inner temperature sensor was placed on the outer surface of the rubber sleeve to indicate the sample temperature. The inlet pore pressure pipe was connected via a three-way valve to a vacuum pump, a methane gas cylinder (with pressure regulator) and a brine reservoir. A syringe pump was used to inject brine into the sample in a controlled manner, while the temperature of the system was regulated by a controlled cooling circuit.

The inner cell was configured for ultrasonic pulse-echo measurements of P- and S-wave velocity (V_p and V_s) with an accuracy ± 0.3% (Best et al., 1994). The inner rubber sleeve that prevents

direct contact between the mineral oil, used as confining fluid, and the rock sample is perforated by 16 electrodes for electrical resistivity measurements (North et al., 2013). Under typical operating conditions, the resistivity measurement error is ≤ 0.1% (at A/C frequencies 1 - 500 Hz) for samples in the electrical resistivity range 1 - 100 Ω m (North et al., 2013). This system does not allow simultaneous ultrasonic and electrical measurements because the ultrasonic system gives a ground path for the electrical system. The resistivity system took nearly one hour for each measurement, so we have fewer resistivity measurements.

2.4 Synchrotron X-ray CT imaging

We designed and manufactured a miniature cylindrical hydrate rig to fit the SRXCT stage at the TOMCAT beamline, Swiss Light Source (SLS), Switzerland. It was manufactured from monolithic PEEK plastic by precision lathe and drilling machines (see Figure 2b). The rig had an internal diameter of 2 mm, a wall thickness of 0.8 mm and sample scan height of 10 mm (23 mm total height). Internal and external thermocouples were installed below the scan zone to measure the temperature throughout the experiment. In order to reduce the temperature within phase boundary, cooled nitrogen gas was blown at 5L/min onto the sample using CryojetXL (Oxford Instruments). The temperature of the jet was initially calibrated by varying discharge and N_2 gas temperature to provide stable 2°C sample internal temperature. The gas hydrate formation and dissociation process was imaged through computed tomography (CT) using monochromatic X-rays from a synchrotron source (TOMCAT SLS). Beam energy of 21 keV, 81 mm propagation distance, 200 ms exposure time (1501 projections over 180° sample rotation) with 1.25 x, 4 x and 10 x objectives were chosen after trial runs to obtain images at 1.625 µm, 0.625 µm and 0.325 µm voxel size respectively. The transmitted and refracted x-rays from the sample was converted to visible light by LuAG:Ce scintillator, thereafter magnified and recorded by sensitive CCD cameras (2560x2160 pixels). Figure2b shows details of the hydrate rig including the pore fluid injection system and temperature control. The TOMCAT facility uses phase shifts of the X-rays as they pass through the sample (Fitzgerald, 2000; Stampanoni et al., 2002). We used the phase reconstruction algorithm described by Paganin et al. (2002). Reconstructed CT data were post-processed using ImageJ and visualized using Amira-Avizo® 3D software.

We calibrated the grey scale values in the CT data to known standard densities (sand, brine, hydrate and methane gas; e.g., Kneafsey et al., 2007). The grey scale intensity represents the extent to which the X-ray signals are attenuated. Different material in the sample, attenuate the X-ray signal to a different extent, resulting in different grey scale intensity. The grey scale intensities are mainly dependent on density of the material and beam energy but are also slightly influenced by other factors like atomic number, reconstruction algorithm (Koeberl, 2002; Phillips & Lannutti, 1997). Following the approach of previous studies (e.g., Kneafsey et al., 2007, Iassonov et al., 2009), the grey scale values were calibrated with density of sand, brine and methane gas (2650 kg/m^3, 1025 kg/m^3, 18 kg/m^3) using scans with no hydrate. This provides a relation between gray scale intensity and density. The grey scale intensity range for hydrate was derived by using this relationship with a hydrate density of 925 kg/m^3. By choosing the grey scale intensity range derived from associated material density (Figure 4c), we segmented the 2D slices stack to obtain separate sand, brine, hydrate and methane gas as binary images file stacks (e.g., Iassonov et al., 2009). We then used these individual stacks to estimate the volume of gas, hydrate and water. Porosity was calculated by adding the volume of gas, water and hydrate. An example of reconstructed 2D slice at two different hydrate formation time along with its grey scale intensity profile drawn between two sand particles passing a methane bubble and brine within the pore between these particles is shown in Figure 4. The density based boundary lines (Figure 4c) clearly shows ability of this segmentation technique to distinguish different phases especially between methane hydrate, gas (between 20-60μ profile length) and brine (65-75μ profile length) within the pore space. This segmentation allows a range of grey scale for each component (sand, brine, methane gas and hydrate) to be highlighted, for enhanced visual contrast. For example, Rees et al. (2011) studied a natural gas hydrate bearing sediment sample collected offshore India (NGHP-1) using this segmentation technique.

Each scan took around 10 mins. However, as hydrate formation is a relatively slow process taking between 40-50 hours, and we had to trade-off between storage and analysis capacity and frequency of scans able to capture the main changes during hydrate formation, we decided a scan frequency of ~30 minutes. We increased the scan frequency to the maximum possible (~15 mins) during rapid hydrate formation, and reduced the scan frequency during other times (1-3 hours). See supplementary information for additional scans (Movie S1, Figure S2).

2.5 Rock Physics Model

We used the hydrate bearing effective sediment (HBES) model of Marín-Moreno et al. (2017) to relate changes in velocity to changes in hydrate saturation and morphology (at least for pre-conceived, idealised morphologies of cementing, pore-floating hydrate discussed in Section 1). HBES model calculates frequency dependent (from seismic to ultrasonic) P- and S-wave velocity and attenuation of hydrate bearing sediment (Figure 5). It was derived from the previous HEG (Hydrate Effective Grain) model of Best et al. (2013) which adapted extant static (zero frequency, broadly equivalent to seismic frequencies) velocity models for hydrate morphologies (cementing, pore-floating, pore-bridging) by Ecker et al. (1998) and Helgerud et al. (1999) for the purpose of predicting attenuation and velocity dispersion, using model concepts developed by Leurer & Brown (2008) and Leurer (1997) for clay-squirt flow attenuation in marine sediments. The central idea is that hydrate can be treated as an effective medium of solid hydrate with fluid inclusions (similar to clay assemblages in Leurer et al. (1997)). During the passing of an elastic wave, the different elastic compliances of the porous medium host (e.g. sand grain framework) and the porous hydrate grains creates local fluid pressure gradients between the hydrate inclusions and the sand frame pores, leading to viscous fluid flow (squirt flow) of water, and associated wave energy loss. The squirt flow element is embedded in the Biot-Stoll global fluid flow model (Biot, 1956b, 1956a)(Biot, 1956b, 1956a)(Biot, 1956b, 1956a)(Biot, 1956b, 1956a)(Biot, 1956b, 1956a)(Biot, 1956b, 1956a)(Biot, 1956b, 1956a)(Biot, 1956b, 1956a)(Biot, 1956b, 1956a)(Biot, 1956b, 1956a)(Biot, 1956b, 1956a)(Biot, 1956b, 1956a)(Biot, 1956a, 1956b) giving an effective medium solution for frequency-dependent P- and S-wave velocity and attenuation in hydrate-bearing sediments and rocks, as a function of both hydrate content (saturation) and the specific morphologies above.

The HBES model extended the HEG model to include additional loss mechanisms identified from the pore-scale hydrate morphology, and the coexistence of gas, water and hydrate. In addition to the HEG model squirt flow due to hydrate grain fluid inclusions described above (termed sub-micro squirt flow in the HBES model), the HBES model introduces another form of squirt flow (termed micro squirt flow) due to the low aspect ratio pores that are created during

hydrate formation between the hydrate grains and the sand frame pore walls (Figure 5). The model incorporates gas bubbles resonance effects according to Smeulders and van Dongen (1997) (Figure 5).

The HBES model was developed for hydrate growing in the sediment pore space, and do not account for grain displacing hydrate. The HBES model accounted for pore-floating and cementing (grain coating and contact cementing) morphologies. We adapted the HBES model for pore-bridging hydrate using the approach of Ecker et al., (2000), which considers that pore bridging hydrate reduces the porosity and affects the elastic properties of the solid phase. All the HBES model input parameters are given in Table 1. As our Berea sandstone sample had 1.7 volume % illite and 3.4 volume % k-feldspar, we first used the Voigt–Reuss–Hill average to calculate the bulk and shear moduli of the grains, which were then used as inputs to the HBES model. The saturation of hydrate, gas and brine in the pore space was calculated from changes in pore pressure and temperature using the thermodynamics approach of Sahoo et al. (2018). This saturation calculation showed the presence of co-existing gas even at maximum hydrate saturation, and hence we included the bubble resonance effect of the HBES model. The pore size in our Berea sample varied from 11 μm to 73 μm, measured from SR-XCT at TOMCAT, SLS Switzerland (Sahoo et al., 2018), and we choose to use 10 and 20 μm bubble radii in the HBES model. Based on observations from the synchrotron images we expect that, initially, the bubble would almost completely fill the pore, and with the formation of hydrate, the bubble size would reduce. The aspect ratio and concentration of pores created during hydrate formation were chosen based on the values used in Marín-Moreno et al. (2017). The concentration of inclusions in hydrate was set to zero, as they have a negligible effect on V_p in our measurement frequency band (Marín-Moreno et al., 2017).

3.0 Results and Discussions

3.1 Synchrotron imaging of hydrate formation.

After carefully inspecting the extensive X-ray CT dataset (9 TB of data), we selected the images that could best describe the key hydrate formation processes that we observed (Figure 6). The 3D volume reconstructed time-lapse sequence in Figure 6 demonstrates the evolution of hydrate

morphology within the pore space. A full time-lapse sequence of 2D slices is shown in the supplementary information (Movie S1, Figure S2). Hydrate grows initially as a shell around gas bubbles scattered throughout the pore space, as also reported for methane hydrate formation in water without sediments (e.g., Klapp et al., 2012). The gas is sparsely distributed as sub-spherical "bubbles" with a range of sizes; some gas bubbles almost completely fill the pores, while others occupy part of the pore only (Figure 6a, b). Hydrate formation starts at the gas-water interface as expected. Hydrate films that develop on bubbles at some point seem to rupture, and the trapped gas escapes (Figure 6c, d). Hydrate formation consumes methane, reducing the pore fluid pressure, and is also an exothermic reaction. The resulting pressure drop and temperature increase may lead to bubble expansion and/or rupture of the hydrate shell. Some of the escaped gas forms smaller bubbles which later forms more hydrate (Figure 6 c, d). Hydrate growing in adjacent pores then starts to coalesce as the pores are further filled with hydrate, creating an inter-pore hydrate framework interlocking with the sand grain framework (Figure 6c, d). The spherical shapes of bubbles distort due to further hydrate growth into the gas bubble. Ultimately, the gas remains as isolated pockets surrounded by hydrate, while hydrate occupies most of the pore space in patches throughout the volume (Figure 6e, f). Such distorted bubble shapes and uneven, porous hydrate distribution could have an impact on elastic wave propagation mechanisms (Section 3.3). The presence of such pockets of gas confirms the hypothesis of co-existence of water, hydrate and methane gas proposed by Sahoo et al. (2018) from electrical resistivity and thermodynamic calculations. A film of water is evident between hydrate and sand even at maximum hydrate saturation (Figure 6e).

The highest hydrate content occurs where the porosity is highest, but the lowest hydrate content is not where the porosity is lowest (Figure 7).The depth variation of S_h increases as the average S_h increases (Figure 7); at 45h 10 min, S_h varies between 38 and 60%, about a mean saturation of 44%. Even though the gas was injected from below, the maximum gas hydrate saturation occurs towards the upper part of sample. We installed two thermocouples to measure internal (just below the scan zone) and external (room) temperature; we did not observe any temperature increase in the sample during hydrate formation.

We note the following caveats when comparing the results of synchrotron imaging to the ultrasonic experiments in the sections below. Although the sample’s porosity, permeability, and

size are different, it may not affect observed hydrate morphologies as described in Section 2.1. The inlet pipe in the synchrotron imaging rig is in the center of the sample, while it is off-center for the ultrasonic rig (Figure 2). The ratio of diameter of each sample to that of the pore fluid inlet pipe is 24.5 for the ultrasonic rig and 15.7 for the imaging rig, respectively. These differences might have affected the initial distribution of the gas and hydrate in the sample. The off-center position of the inlet pipe in the ultrasonic rig might have caused a less homogenous distribution of gas in the sample compared to the synchrotron rig. However, as hydrate formation in both experiment was from gas bubbles in excess water condition, we expect the observed hydrate formation morphologies to be similar in natural hydrate systems, especially for coarse-grained sediments that are fed by free gas from below. For example, porous hydrate have been found in the southern summit of Hydrate Ridge (offshore Oregon, USA) which likely formed when methane hydrate film coated gas bubbles moved upwards within the sediments and coalesced together (Suess et al., 2001). Such porous hydrates have also been found offshore Nigeria (Sultan et al., 2014).

3.2 Ultrasonic velocity changes during hydrate formation and dissociation.

The cooling of the system to 5 ˚C generated a reduction in pore pressure as shown in Figure 3, points ABC. The pressure drop can be explained mainly by hydrate formation, with some contribution from methane gas contraction and increased gas solubility between AB. A slight increase in temperature can also be seen in Figure 3a between points B and C, caused by the exothermic reaction of hydrate formation (Hwang et al., 1990). Figure 8 shows rapidly increasing P- and S-wave velocities (V_p and V_s, respectively) during the initial 10 hours of hydrate formation, followed by a more gradual increase thereafter. Once hydrate formation ceased, indicated by the end of the pore pressure decrease at about 260 hours (Figure 3b), the system was left at that pressure and temperature for several hours to ensure complete hydrate formation. The asymptotic behavior of the pore pressure in Figure 3b, and of V_p and V_s in Figures 8a,b is evidence that no further hydrate formation took place (e.g., Waite et al., 2004). As the system was taken out of hydrate stability by heating, there was an increase in pore pressure (trajectory CD in Figure 3) and a decrease in V_p and V_s (Figure 8 c, d).

The time taken to reach the cycle's maximum velocity, and associated maximum hydrate saturation, is longer in the first cycle than in subsequent cycles, which may be due to a methane hydrate formation memory effect (Ohmura et al., 2003; Sloan & Koh, 2007; Takeya et al., 2000). The memory effect is related to survival of meta stable clathrate clusters of water after hydrate dissociation making subsequent hydrate nucleation more likely (Rodger, 2006; Sloan & Koh, 2007). As some researchers dispute the memory effect(e.g., Buchanan et al., 2005), we offer an additional explanation. We propose this time reduction may be due to an increase in the contact area of the gas/brine interfaces after the first formation and dissociation cycle, associated with a more even distribution of smaller gas bubbles, as observed in the synchrotron images. Smaller spheres have a larger surface area per unit volume than larger ones, and this change could increase the total reaction surface area.

3.3 Morphology of hydrate from ultrasonic velocity

3.3.1 Changes in gradient of change of velocity during hydrate formation

The observed increases in V_p and V_s in Figure 8a & b depend on both hydrate saturation and morphology. Here, we apply the hydrate bearing effective sediment (HBES) model of Marín-Moreno et al. (2017) to our experimental results with the aim of relating changes in velocity to changes in hydrate saturation and morphology.

Small increases in V_p and V_s for hydrate saturations (S_h) up to about 5% are well represented by implementing a pore-floating hydrate morphology in the HBES model (Figure 9). As hydrate saturation increases above 5%, the observed V_p increases more steeply and approaches the pore-bridging morphology model results at about S_h = 15%. It is generally accepted that when saturation of pore-floating hydrate increases, it eventually starts bridging the pores (Priest et al., 2009; Waite et al., 2009). Above S_h = 15%, the gradient of V_p becomes smaller, and diverges below the predicted pore-bridging increase of the HBES model. This observation indicates that, for saturations above 15%, only a small proportion of the newly formed hydrate is adding to bridging of the pores. Similarly, V_s continues to track the pore-floating HBES model up to S_h of 5%. For $S_h > 5\%$, in contrast to V_p, V_s falls below the HBES model for pore-bridging morphology. A possible explanation is that when hydrate fills the pores in our experiments, it does not make solid-solid bonds to the host sand grains, as assumed in the HBES pore-bridging model. Instead, a thin, bound water layer may exist between the water wet sand grains and the hydrate, as observed in our synchrotron images (Figure 6). The presence of the water film could increase the Berea's frame bulk modulus in a similar manner to the pore-bridging model, but not the frame shear modulus. Only when sufficient hydrate has grown to interlock the sand grains would the frame shear modulus increase, and then still less than for solid-solid contacts. This phenomenon could explain the rise of V_s above the pore-floating model line, but below the pore-bridging model line.

There is a steep increase in V_s around S_h = 23% in Figure 9b, with a less pronounced increase in V_p (Figure 9a). This behavior is also seen in Figure 8. The increase in Vs with hydrate formation in cycles 1 and 3 shows two distinct segments, with an initial increase followed by a plateau, followed by a renewed velocity increase up to a plateau at the maximum V_s (Figure 8b). Cycles 1

and 3 can be considered as the first cycles at each differential pressure, 10 MPa for cycle 1 and 55 MPa for cycle 3. The steep increase in cycle 1 and 3 (at 39 hours for cycle 1, and 47 hours for cycle 3, in Figure 8b), might occur when sufficient hydrate has grown to interlock extensively the sediment. The sudden increase in V_s could indicate a threshold of interlocking when the rock frame shear modulus is stiffened significantly. The HBES model does not consider this new inter-pore hydrate framework morphology..

While we expect different hydrate formation/dissociation rates in Berea and Leighton Buzzard sand (e.g. hydrate formation of about 80 & 45 hours respectively), we would expect the pore scale morphological evolution to be similar in both the experiments (as discussed in Section 2.1). The coalescence of hydrate from adjacent pores creating an inter-pore hydrate framework, which interlocks the host grains (Figure 6) could be linked with this rapid increase in V_s seen in Figures 8 & 9. Such a steep increase is less prominent in V_p (Figure 9) suggesting that the increase in bulk modulus is dominated by replacement of pore-fluid with pore-bridging hydrate, irrespective of whether the hydrate significantly interlocks or not.

For cycle 3, electrical resistivity also shows a similar steep increase at S_h = 21% in Figure 8. We do not have resistivity measurements between S_h of 1% and 21%, but it is clear that steep increase in velocity matches with that of resistivity (Figure 10). The steep increase in resistivity can be also be explained by coalescence of hydrate from adjacent pores creating an inter-pore hydrate framework. When hydrate from adjacent pores coalesces, they might block electrical current conduction paths, causing a rapid increase in resistivity. The gradient of increase in resistivity seems to decrease at higher hydrate saturations, reaching a maximum at S_h = 25%.

A possible explanation for the absence of such behavior in cycles 2 and 4 could be a reduction in gas bubble size that results in pore-bridging aggregates formed by smaller hydrate “grains”. Hydrate forms on gas bubble surfaces, and smaller gas bubbles would result in smaller hydrate grains. With more hydrate formation, such hydrate grains would aggregate to eventually bridge the pores and interlock the rock frame, as discussed earlier. For a given volume of hydrate, smaller hydrate grains will form hydrate aggregates with more discontinuities than larger hydrate grains, resulting in a smaller shear modulus. Hence, aggregation of smaller hydrate grains may lead to a weaker effect on V_s. As discussed earlier, hydrate dissociation can lead to more uniform

distribution of methane gas and a reduction in bubble size. So it is possible that bubble size is lower in cycles 2 and 4 than in cycles 1 and 3. The patterns of change of V_s and V_p for first and third cycles are similar, and the patterns are also similar between the second and fourth cycle (Figure 8 a, b). As expected, the magnitude of changes is higher for lower differential pressures (cycles 1 and 2).

While our experiments show transitions of the geophysical properties at specific hydrate saturations in our experiments, it is likely that such transitions occur at different hydrate saturations depending on sediment type and hydrate formation method. In Section 1, we discussed the results of Priest et al., (2009) and Yun et al., (2005), which show similar transitions at slightly different saturations. (S_h = 30% - Priest et al., 2009; S_h = 40% - Yun et al., 2005).

3.3.2 Possible effect of water film on wave velocities

The observation that V_p matches the pore-bridging HBES model but not V_s, likely due to the presence of water films between hydrate and sand, adds another level of complexity to the effect of hydrate morphology on elastic wave velocities. We no longer should view hydrate as pore-bridging in the sense of solid-solid contacts, as developed initially (e.g., Ecker et al., 2000; Priest et al., 2009).We should account also for the presence of a water film between hydrate and sediment surface as seen in Figure 6 and other studies (e.g., Bonnefoy et al., 2005; Chaouachi et al., 2015; Sell et al., 2018; Tohidi et al., 2001). Gas hydrate bearing sediment should be viewed as a three-phase system of interlocking solid hydrate and host grain frameworks separated by water. Indeed, the presence of a water film between sand grains and hydrate is consistent with the Leclaire et al. (1994) three phase Biot model adapted for hydrate by Guerin & Goldberg (2005) and Carcione & Tinivella (2000). Best et al. (2013) found that this model gave reasonable predictions of shear wave attenuation. This observation also implies that the hydrate cementing model concept may need to be revisited to include this water layer effect (e.g., Chaouachi et al., 2015; Sell et al., 2018; Tohidi et al., 2001).

3.3.3 Different maximum velocity in different hydrate formation cycles

We see higher maximum V_p and V_s for cycle 1 than for cycle 2, while those for cycle 3 and 4 are similar (Figure 8). The percentage difference in maximum V_p between cycles 1 and 2 is about double that of Vs. Different maximum velocities between cycles 1 and 2 can be explained by (i) higher hydrate saturation in cycle 1 than in cycle 2, and/or (ii) reduction in bubble size in cycle 2. In cycle 1, S_h could not be calculated due to a malfunctioning pressure gauge, and in cycles 2, 3 and 4 the maximum S_h values were 23%, 26% and 25%, respectively. The HBES model shows that a slight increase of pore-bridging hydrate equal to S_h of 3 to 4% could account for the observed discrepancies in maximum V_p and V_s between cycles 1 and 2 (Figure 9). A reduction in bubble size can cause a similar effect. The latter mechanism is also consistent with a redistribution of methane gas and a change in bubble size occurring during hydrate dissociation and reformation, as discussed above.

3.4 Effect of differential pressure

The rate of change in V_p and V_s with S_h, for S_h of 10% to 15%, is much higher at a differential pressure of 10 MPa, than at 55 MPa (Figure 11). The onset of the rapid increase in V_p and V_s occurs at a lower S_h at 10 MPa than at 55 MPa. This behavior might be due to the presence of microcracks at 10 MPa that are mostly closed at 55 MPa (e.g., Prasad and Manghnani, 1997). When the microcracks are open, hydrate formation is likely to cause a much more dramatic initial stiffening of the rock frame bulk moduli than when the microcracks are closed at higher pressures, leading to a steeper increase in V_p and V_s, because the frame moduli are initially weaker. This effect is similar in magnitude to the normal velocity-pressure dependence reported for Berea and similar sandstones with microcracks, where velocity increases more rapidly at lower than at higher pressures (Eberhart-Phillips et al., 1989; Prasad & Manghnani, 1997). The effect of microcracks is evident as the initial (start of hydrate formation cycle) V_p and V_s for the first and second cycles are lower than those for the third and fourth cycles (Figure 8).

4 Conclusions

Estimates of hydrate content, and of hydrate related geohazards, from seismic data depend on our understanding of the morphology and formation process of non-cementing hydrate in porous media. From our experimental observations, we can conclude the following:

1. Our time resolved/lapse (4D) SR-XCT images show that hydrate grows initially in a pore-floating morphology and transitions to a pore-bridging morphology. Then, eventually, it forms an inter-pore hydrate framework that interlocks with the sand grain framework, although separated by water films. To our knowledge, this is the first observation of such a methane hydrate morphology existing in a porous medium.

2. The SR-XCT images confirm the occurrence of a hydrate film around methane gas bubbles, trapping gas inside, as the mechanism of co-existence of gas with hydrate under hydrate stability conditions. SR-XCT images show that water films occur between hydrate and sand when using methane and brine for hydrate formation. They also confirm the previously inferred porous nature of hydrate. Using rock physics modeling, we were able to link these morphological transitions to changes in the rate of increase of P- and S-wave velocity with hydrate saturation.

3. The size of gas bubbles forming hydrate has a significant effect on velocities. The presence of smaller gas bubbles can result in reaching maximum hydrate saturations sooner than with large gas bubbles because there is an increase in surface reaction area. Smaller gas bubbles also result in smaller hydrate grains, and when they aggregate the number of discontinuities is larger than for larger hydrate grains, resulting in lower shear modulus and velocity.

4. While P-wave velocities match the modeled velocity for pore-bridging hydrate, S-wave velocities are higher than the pore-floating model and lower than the pore-bridging model, likely due to presence of water films between hydrate and the rock frame. Both ultrasonic velocities and imaging results indicate that hydrate-bearing sediment is a system of interlocking solid hydrate and host grain frameworks separated by water films, with isolated pockets of gas within the hydrate.

These observations are likely to be typical of natural hydrate-bearing sediments charged by gas from below. Such inter-pore hydrate framework and co-existing gas, if widespread in nature, should be considered when estimating *in situ* hydrate contents from elastic wave velocities.

Acknowledgments

The authors are grateful to the Swiss Light Synchrotron Radiation facility for access to the TOMCAT-X02DA beamline, and for the assistance of Dr. Anne Bonnin and Mr. Thomas Steigmeier. Thanks to the μ-VIS facility at the University of Southampton for image analysis capability, and particularly to Prof. Ian Sinclair for his help with the proposal to TOMCAT. We acknowledge Dr. Gaowei Hu for his input at the start of the experiments and lab scale X-ray CT imaging of hydrate formation. We acknowledge funding from the UK Natural Environment Research Council (grant no NE/J020753/1). Madhusudhan was supported by the NERC Landslide-Tsunami risk to the UK (NE/K00008X/1). T. A. Minshull was supported by a Royal Society Wolfson Research Merit award. We are grateful to two anonymous reviewers for their valuable comments. The experimental data is available at the National Geoscience Data Centre, UK under the grant NE/J020753/1.

References

Archer, D., Buffett, B., & Brovkin, V. (2009). Ocean methane hydrates as a slow tipping point in the global carbon cycle. *Proceedings of the National Academy of Sciences of the United States of America*, *106*(49), 20596–601. https://doi.org/10.1073/pnas.0800885105

Attias, E., Weitemeyer, K. A., Minshull, T. A., Best, A. I., Sinha, M., Jegen-Kulcsar, M., … Berndt, C. (2016). Controlled-source electromagnetic and seismic delineation of subseafloor fluid flow structures in a gas hydrate province, offshore Norway. *Geophysical Journal International*, *206*(2), 1093–1110. https://doi.org/10.1093/gji/ggw188

Best, A. I., Priest, J. A., Clayton, C. R. I., & Rees, E. V. L. (2013). The effect of methane hydrate morphology and water saturation on seismic wave attenuation in sand under shallow sub-seafloor conditions. *Earth and Planetary Science Letters*, *368*, 78–87. https://doi.org/10.1016/j.epsl.2013.02.033

Best, A. I., Mccann, C., & Sothcott, J. (1994). The relationships between the velocities , attenuations and petrophysical properties of reselvoi r sedimentary rocksl. *Geophysical Prospecting*, 151–178.

Biot, M. A. (1956a). Theory of Propagation of Elastic Waves in a Fluid-Saturated Porous Solid. I. Low-Frequency Range. *The Journal of the Acoustical Society of America*, *28*(2), 168–178. https://doi.org/10.1121/1.1908239

Biot, M. A. (1956b). Theory of Propagation of Elastic Waves in a Fluid-Saturated Porous Solid. II. Higher Frequency Range. *The Journal of the Acoustical Society of America*, *28*(2), 179–191. https://doi.org/10.1121/1.1908241

Bonnefoy, O., Gruy, F., & Herri, J. M. (2005). Van der Waals interactions in systems involving gas hydrates. *Fluid Phase Equilibria*, *231*(2), 176–187. https://doi.org/10.1016/j.fluid.2005.02.004

Boswell, R., & Collett, T. S. (2011). Current perspectives on gas hydrate resources. *Energy Environ. Sci.*, *4*(4), 1206–1215. https://doi.org/10.1039/C0EE00203H

Boswell, R., Shelander, D., Lee, M. W., Latham, T., Collett, T. S., Guerin, G., … Goldberg, D. (2009). Occurrence of gas hydrate in Oligocene Frio sand: Alaminos Canyon Block 818: Northern Gulf of Mexico. *Marine and Petroleum Geology*, *26*(8), 1499–1512. https://doi.org/10.1016/j.marpetgeo.2009.03.005

Buchanan, P., Soper, A. K., Thompson, H., Westacott, R. E., Creek, J. L., Hobson, G., & Koh, C. A. (2005). Search for memory effects in methane hydrate: Structure of water before hydrate formation and after hydrate decomposition. *Journal of Chemical Physics*, *123*(16). https://doi.org/10.1063/1.2074927

Carcione, J. M., & Tinivella, U. (2000). Bottom-simulating reflectors: Seismic velocities and AVO effects. *Geophysics*, *65*(1), 54–67. https://doi.org/10.1190/1.1444725

Chand, S., Minshull, T. A., Priest, J. A., Best, A. I., Clayton, C. R. I., & Waite, W. F. (2006). An effective medium inversion algorithm for gas hydrate quantification and its application to laboratory and borehole measurements of gas hydrate-bearing sediments. *Geophysical Journal International*, *166*(2), 543–552. https://doi.org/10.1111/j.1365-246X.2006.03038.x

Chaouachi, M., Falenty, A., Sell, K., Enzmann, F., Kersten, M., Haberthür, D., & Kuhs, W. F. (2015). Microstructural evolution of gas hydrates in sedimentary matrices observed with synchrotron X-ray computed tomographic microscopy. *Geochemistry, Geophysics, Geosystems*, *16*(6), 1711–1722. https://doi.org/10.1002/2015GC005811

Collett, T. S. (2001). A Review of Well-Log Analysis Techniques Used to Assess Gas-Hydrate-Bearing Reservoirs. In *Natural Gas Hydrates: Occurrence, Distribution, and Detection* (pp.

189–210). American Geophysical Union. https://doi.org/10.1029/GM124p0189

Collett, T. S., Riedel, M., Boswell, R., Presley, J., Kumar, P., Sathe, A., … Lall, M. V. (2015). *Indian National Gas Hydrate Program Expedition 01 report*. *Scientific Investigations Report*. Reston, VA. https://doi.org/10.3133/sir20125054

Cook, A. E., & Waite, W. F. (2018). Archie's Saturation Exponent for Natural Gas Hydrate in Coarse-Grained Reservoirs. *Journal of Geophysical Research: Solid Earth*. https://doi.org/10.1002/2017JB015138

Dai, S., Santamarina, J. C., Waite, W. F., & Kneafsey, T. J. (2012). Hydrate morphology: Physical properties of sands with patchy hydrate saturation. *Journal of Geophysical Research*, *117*(B11), B11205. https://doi.org/10.1029/2012JB009667

Daigle, H., Cook, A., & Malinverno, A. (2015). Permeability and porosity of hydrate-bearing sediments in the northern Gulf of Mexico. *Marine and Petroleum Geology*, *68*, 551–564. https://doi.org/10.1016/j.marpetgeo.2015.10.004

Doveton, J. H. (2001). All Models Are Wrong , but Some Models Are Useful : " Solving " the Simandoux Equation Prolog : The Archie Equation.

Eberhart-Phillips, D., Han, D.-H., & Zoback, M. D. (1989). Empirical relationships among seismic velocity, effective pressure, porosity, and clay content in sandstone. *Geophysics*, *54*(1), 82–89. https://doi.org/10.1190/1.1442580

Ecker, C., Dvorkin, J., & Nur, A. (1998). Sediments with gas hydrates: Internal structure from seismic AVO. *Geophysics*, *63*(5), 1659–1669. https://doi.org/10.1190/1.1444462

Ecker, C., Dvorkin, J., & Nur, A. (2000). Estimating the amount of hydrate and free gas from surface seismic. *Geophysics*, *65*(2), 565–573. https://doi.org/10.1190/1.1820496

Edwards, R. N. (1997). On the resource evaluation of marine gas hydrate deposits using sea-floor transient electric dipole-dipole methods. *Geophysics*, *62*(1), 63–74. https://doi.org/10.1190/1.1444146

Ellis, M. H. (2008). *Joint Seismic and Electrical Measurements of Gas Hydrates in Continental Margin Sediments*. PhD thesis, University of Southampton. Retrieved from http://eprints.soton.ac.uk/id/eprint/63293

Fitzgerald, R. (2000). Phase-Sensitive X-Ray Imaging. *Physics Today*, *53*(7), 23–26. https://doi.org/10.1063/1.1292471

Fujii, T., Suzuki, K., Takayama, T., Tamaki, M., Komatsu, Y., Konno, Y., … Nagao, J. (2015). Geological setting and characterization of a methane hydrate reservoir distributed at the first offshore production test site on the Daini-Atsumi Knoll in the eastern Nankai Trough, Japan. *Marine and Petroleum Geology*, *66*, 310–322. https://doi.org/10.1016/j.marpetgeo.2015.02.037

Gorman, A. R., Holbrook, W. S., Hornbach, M. J., Hackwith, K. L., Lizarralde, D., & Pecher, I. (2002). Migration of methane gas through the hydrate stability zone in a low-flux hydrate province. *Geology*, *30*(4), 327. https://doi.org/10.1130/0091-7613(2002)030<0327:MOMGTT>2.0.CO;2

Goswami, B. K., Weitemeyer, K. A., Minshull, T. A., Sinha, M. C., Westbrook, G. K., Chabert, A., … Ker, S. (2015). A joint electromagnetic and seismic study of an active pockmark within the hydrate stability field at the Vestnesa Ridge, West Svalbard margin. *Journal of Geophysical Research: Solid Earth*, *120*(10), 6797–6822. https://doi.org/10.1002/2015JB012344

Guerin, G., & Goldberg, D. (2005). Modeling of acoustic wave dissipation in gas hydrate-bearing sediments. *Geochemistry, Geophysics, Geosystems*, *6*(7), 1–16.

https://doi.org/10.1029/2005GC000918

Guerin, G., Goldberg, D., & Meltser, A. (1999). Characterization of in situ elastic properties of gas hydrate-bearing sediments on the Blake Ridge. *Journal of Geophysical Research: Solid Earth*, *104*(B8), 17781–17795. https://doi.org/10.1029/1999JB900127

Han, T., Best, A. I., Sothcott, J., North, L. J., & MacGregor, L. M. (2015). Relationships among low frequency (2Hz) electrical resistivity, porosity, clay content and permeability in reservoir sandstones. *Journal of Applied Geophysics*, *112*, 279–289. https://doi.org/10.1016/j.jappgeo.2014.12.006

Handa, Y. P. (1990). Effect of hydrostatic pressure and salinity on the stability of gas hydrates. *The Journal of Physical Chemistry*, *94*(6), 2652–2657. https://doi.org/10.1021/j100369a077

Helgerud, M. B., Dvorkin, J., Nur, A., Sakai, A., & Collett, T. S. (1999). Elastic-wave velocity in marine sediments with gas hydrates: Effective medium modeling. *Geophysical Research Letters*, *26*(13), 2021–2024. https://doi.org/10.1029/1999GL900421

Holland, M., Schultheiss, P., Roberts, J., & Druce, M. (2008). Observed Gas Hydrate Morphologies in Marine Sediments. In *6th International Conference on Gas Hydrates*.

Hu, G., Ye, Y., Liu, C., Best, A. I., & Li, C. (2014). Gas Hydrate Distribution in Sediment Pore Space and Its Impact on Acoustic Properties of Hydrate-Bearing Sediments.

Iassonov, P., Gebrenegus, T., & Tuller, M. (2009). Segmentation of X-ray computed tomography images of porous materials: A crucial step for characterization and quantitative analysis of pore structures. *Water Resources Research*, *45*(9), 1–12. https://doi.org/10.1029/2009WR008087

Jung, J. W., Espinoza, D. N., & Santamarina, J. C. (2010). Properties and phenomena relevant to CH 4 -CO 2 replacement in hydrate-bearing sediments. *Journal of Geophysical Research*, *115*(B10), B10102. https://doi.org/10.1029/2009JB000812

Kerkar, P. B., Horvat, K., Jones, K. W., & Mahajan, D. (2014). Imaging methane hydrates growth dynamics in porous media using synchrotron X-ray computed tomography. *Geochemistry Geophysics Geosystems*, *15*, 4759–4768. https://doi.org/10.1002/2014GC005373

Klapp, S. A., Enzmann, F., Walz, P., Huthwelker, T., Tuckermann, J., Schwarz, J. O., … Brewer, P. G. (2012). Microstructure characteristics during hydrate formation and dissociation revealed by X-ray tomographic microscopy. *Geo-Marine Letters*, *32*(5–6), 555–562. https://doi.org/10.1007/s00367-012-0276-0

Kleinberg, R. L., Flaum, C., Griffin, D. D., Brewer, P. G., Malby, G. E., Peltzer, E. T., & Yesinowski, J. P. (2003). Deep sea NMR: Methane hydrate growth habit in porous media and its relationship to hydraulic permeability, deposit accumulation, and submarine slope stability. *Journal of Geophysical Research: Solid Earth*, *108*(B10). https://doi.org/10.1029/2003JB002389

Kneafsey, T. J., Tomutsa, L., Moridis, G. J., Seol, Y., Freifeld, B. M., Taylor, C. E., & Gupta, A. (2007). Methane hydrate formation and dissociation in a partially saturated core-scale sand sample. *Journal of Petroleum Science and Engineering*, *56*(1–3), 108–126. https://doi.org/10.1016/j.petrol.2006.02.002

Koeberl, C. (2002). High-resolution X-ray computed tomography of impactites. *Journal of Geophysical Research*, *107*, 1–9. https://doi.org/10.1029/2001JE001833

Kumar, A., Sakpal, T., Roy, S., & Kumar, R. (2015). Methane hydrate formation in a test sediment of sand and clay at various levels of water saturation. *Canadian Journal of Chemistry*, *93*(8), 874–881. https://doi.org/10.1139/cjc-2014-0537

Kvenvolden, K. A. (1993). Gas hydrates—geological perspective and global change. *Reviews of Geophysics*, *31*(2), 173. https://doi.org/10.1029/93RG00268

Leclaire, P., Cohen-Ténoudji, F., & Aguirre-Puente, J. (1994). Extension of Biot's theory of wave propagation to frozen porous media. *The Journal of the Acoustical Society of America*, *96*(6), 3753–3768. https://doi.org/10.1121/1.411336

Lee, M. W. (2008). *Models for Gas Hydrate-Bearing Sediments Inferred from Hydraulic Permeability and Elastic Velocities*. Retrieved from https://pubs.usgs.gov/sir/2008/5219/pdf/SIR08-5219_508.pdf

Lee, M. W., & Collett, T. S. (2006). Gas Hydrate and Free Gas Saturations Estimated from Velocity Logs on Hydrate Ridge, offshore Oregon, U.S.A. In *Proceedings of the Ocean Drilling Program, 199 Scientific Results* (Vol. 204, pp. 1–25). Ocean Drilling Program. https://doi.org/10.2973/odp.proc.sr.204.103.2006

Leurer, K. C. (1997). Attenuation in fine-grained marine sediments: Extension of the Biot-Stoll model by the "effective grain model" (EGM). *GEOPHYSICS*, *62*(5), 1465–1479. https://doi.org/10.1190/1.1444250

Leurer, K. C., & Brown, C. (2008). Acoustics of marine sediment under compaction: Binary grain-size model and viscoelastic extension of Biot's theory. *The Journal of the Acoustical Society of America*, *123*(4), 1941–1951. https://doi.org/10.1121/1.2871839

Marín-Moreno, H., Sahoo, S. K., & Best, A. I. (2017). Theoretical modeling insights into elastic wave attenuation mechanisms in marine sediments with pore-filling methane hydrate. *Journal of Geophysical Research: Solid Earth*, *122*(3), 1835–1847. https://doi.org/10.1002/2016JB013577

Milkov, A. V., Dickens, G. R., Claypool, G. E., Lee, Y. J., Borowski, W. S., Torres, M. E., … Schultheiss, P. (2004). Co-existence of gas hydrate, free gas, and brine within the regional gas hydrate stability zone at Hydrate Ridge (Oregon margin): Evidence from prolonged degassing of a pressurized core. *Earth and Planetary Science Letters*, *222*(3–4), 829–843. https://doi.org/10.1016/j.epsl.2004.03.028

Millero, F. J., Chen, C.-T., Bradshaw, A., & Schleicher, K. (1980). A new high pressure equation of state for seawater. *Deep Sea Research Part A. Oceanographic Research Papers*, *27*(3–4), 255–264. https://doi.org/10.1016/0198-0149(80)90016-3

Minagawa, H., Nishikawa, Y., Ikeda, I., Miyazaki, K., Takahara, N., Sakamoto, Y., … Nairta, H. (2008). Characterization of sand sediment by pore size distribution and permeability using proton nuclear magnetic resonance measurement. *Journal of Geophysical Research: Solid Earth*, *113*(7), 1–9. https://doi.org/10.1029/2007JB005403

Miyakawa, A., Saito, S., Yamada, Y., Tomaru, H., Kinoshita, M., & Tsuji, T. (2014). Gas hydrate saturation at Site C0002, IODP Expeditions 314 and 315, in the Kumano Basin, Nankai trough. *Island Arc*, *23*(2), 142–156. https://doi.org/10.1111/iar.12064

North, L. J., Best, A. I., Sothcott, J., & MacGregor, L. (2013). Laboratory determination of the full electrical resistivity tensor of heterogeneous carbonate rocks at elevated pressures. *Geophysical Prospecting*, *61*(2), 458–470. https://doi.org/10.1111/j.1365-2478.2012.01113.x

Nur, A., & Simmons, G. (1969). The effect of saturation on velocity in low porosity rocks. *Earth and Planetary Science Letters*, *7*(2), 183–193. https://doi.org/10.1016/0012-821X(69)90035-1

Ohmura, R., Ogawa, M., Yasuoka, K., & Mori, Y. H. (2003). Statistical Study of Clathrate-Hydrate Nucleation in a Water/Hydrochlorofluorocarbon System: Search for the Nature of

the "Memory Effect." *The Journal of Physical Chemistry B*, *107*(22), 5289–5293. https://doi.org/10.1021/jp027094e

Paganin, D., Mayo, S. C., Gureyev, T. E., Miller, P. R., & Wilkins, S. W. (2002). Simultaneous phase and amplitude extraction from a single defocused image of a homogeneous object. *Journal of Microscopy*, *206*(1), 33–40. https://doi.org/10.1046/j.1365-2818.2002.01010.x

Phillips, D. H., & Lannutti, J. J. (1997). Measuring physical density with X-ray computed tomography. *NDT & E International*, *30*(6), 339–350. https://doi.org/10.1016/S0963-8695(97)00020-0

Prasad, M., & Manghnani, M. H. (1997). Effects of pore and differential pressure on compressional wave velocity and quality factor in Berea and Michigan sandstones. *Geophysics*, *62*(4), 1163–1176. https://doi.org/10.1190/1.1444217

Priegnitz, M., Thaler, J., Spangenberg, E., Schicks, J. M., Schrötter, J., & Abendroth, S. (2015). Characterizing electrical properties and permeability changes of hydrate bearing sediments using ERT data. *Geophysical Journal International*, *202*(3), 1599–1612. https://doi.org/10.1093/gji/ggv245

Priest, J. A., Best, A. I., & Clayton, C. R. I. (2005). A laboratory investigation into the seismic velocities of methane gas hydrate-bearing sand. *Journal of Geophysical Research*, *110*(B4), B04102. https://doi.org/10.1029/2004JB003259

Priest, J. A., Rees, E. V. L., & Clayton, C. R. I. (2009). Influence of gas hydrate morphology on the seismic velocities of sands. *Journal of Geophysical Research: Solid Earth*, *114*(B11), B11205. https://doi.org/10.1029/2009JB006284

Reagan, M. T., & Moridis, G. J. (2008). Dynamic response of oceanic hydrate deposits to ocean temperature change. *Journal of Geophysical Research: Oceans*, *113*(12). https://doi.org/10.1029/2008JC004938

Rees, E. V. L., Priest, J. A. J. A. J. A., & Clayton, C. R. I. (2011). The structure of methane gas hydrate bearing sediments from the Krishna-Godavari Basin as seen from Micro-CT scanning. *Marine and Petroleum Geology*, *28*(7), 1283–1293. https://doi.org/10.1016/j.marpetgeo.2011.03.015

Riedel, M., Collett, T. S., & Malone, M. (2010). Expedition 311 Synthesis: scientific findings. In *Proceedings of the IODP*, *311* (Vol. 311). Integrated Ocean Drilling Program. https://doi.org/10.2204/iodp.proc.311.213.2010

Rodger, P. M. (2006). Methane Hydrate: Melting and Memory. *Annals of the New York Academy of Sciences*, *912*(1), 474–482. https://doi.org/10.1111/j.1749-6632.2000.tb06802.x

Sahoo, S. K., Marín-Moreno, H., North, L. J., Falcon-Suarez, I., Madhusudhan, B. N., Best, A. I., & Minshull, T. A. (2018). Presence and consequences of co-existing methane gas with hydrate under two phase water-hydrate stability conditions. *Journal of Geophysical Research: Solid Earth*. https://doi.org/10.1029/2018JB015598

Schicks, J. M., Naumann, R., Erzinger, J., Hester, K. C., Koh, C. A., & Sloan, E. D. (2006). Phase transitions in mixed gas hydrates: Experimental observations versus calculated data. *Journal of Physical Chemistry B*, *110*(23), 11468–11474. https://doi.org/10.1021/jp0612580

Sell, K., Quintal, B., Kersten, M., & Saenger, E. H. (2018). Squirt flow due to interfacial water films in hydrate bearing sediments. *Solid Earth*, *9*(3), 699–711. https://doi.org/10.5194/se-9-699-2018

Setzmann, U., & Wagner, W. (1991). A New Equation of State and Tables of Thermodynamic Properties for Methane Covering the Range from the Melting Line to 625 K at Pressures up to 100 MPa. *Journal of Physical and Chemical Reference Data*, *20*(6), 1061–1155.

https://doi.org/10.1063/1.555898

Sloan, E. D., & Koh, C. A. (2007). *Clathrate hydrates of natural gases*. New York: CRC Press. Retrieved from https://www.crcpress.com/Clathrate-Hydrates-of-Natural-Gases-Third-Edition/Sloan-Jr-Koh/p/book/9780849390784

Smith, A. J., Flemings, P. B., Liu, X., & Darnell, K. (2014). The evolution of methane vents that pierce the hydrate stability zone in the world's oceans. *Journal of Geophysical Research B: Solid Earth*, *119*(8), 6337–6356. https://doi.org/10.1002/2013JB010686

Spangenberg, E. (2001). Modeling of the influence of gas hydrate content on the electrical properties of porous sediments. *Journal of Geophysical Research: Solid Earth*, *106*(B4), 6535–6548. https://doi.org/10.1029/2000JB900434

Stampanoni, M., Borchert, G., Wyss, P., Abela, R., Patterson, B., Hunt, S., … Rüegsegger, P. (2002). High resolution X-ray detector for synchrotron-based microtomography. *Nuclear Instruments and Methods in Physics Research Section A: Accelerators, Spectrometers, Detectors and Associated Equipment*, *491*(1–2), 291–301. https://doi.org/10.1016/S0168-9002(02)01167-1

Stern, L. A., Lorenson, T. D., & Pinkston, J. C. (2011). Gas hydrate characterization and grain-scale imaging of recovered cores from the Mount Elbert Gas Hydrate Stratigraphic Test Well, Alaska North Slope. *Marine and Petroleum Geology*, *28*(2), 394–403. https://doi.org/10.1016/j.marpetgeo.2009.08.003

Suess, E., Torres, M. E., Bohrmann, G., Collier, R. W., Rickert, D., Goldfinger, C., … Elver, M. (2001). Sea Floor Methane Hydrates at Hydrate Ridge, Cascadia Margin. In *Natural Gas Hydrates—Occurrence, Distribution and Detection* (pp. 87–98). American Geophysical Union. https://doi.org/10.1029/GM124p0087

Sultan, N., Cochonat, P., Foucher, J.-P., & Mienert, J. (2004). Effect of gas hydrates melting on seafloor slope instability. *Marine Geology*, *213*(1–4), 379–401. https://doi.org/10.1016/j.margeo.2004.10.015

Sultan, N., Bohrmann, G., Ruffine, L., Pape, T., Riboulot, V., Colliat, J. L., … Wei, J. (2014). Journal of Geophysical Research : Solid Earth. *Journal of Geophysical Research:Solid Earth*, *119*(December 2011), 2679–2694. https://doi.org/10.1029/2010JB007453.Pockmark

Takeya, S., Hori, A., Hondoh, T., & Uchida, T. (2000). Freezing-memory effect of water on nucleation of CO_2 hydrate crystals. *The Journal of Physical Chemistry B*, *104*(17), 4164–4168. https://doi.org/10.1021/jp993759+

Tohidi, B., Agena, W. F., Clennell, M. Ben, Burgass, R. W., & Biderkab, A. B. (2001). Visual observation of gas-hydrate formation and dissociation in synthetic porous media by means of glass micromodels. *Geology*, *29*(9), 867–870. https://doi.org/10.1130/0091-7613(2001)029

Torres, M. E., Wallmann, K., Tréhu, A. M., Bohrmann, G., Borowski, W. S., & Tomaru, H. (2004). Gas hydrate growth, methane transport, and chloride enrichment at the southern summit of Hydrate Ridge, Cascadia margin off Oregon. *Earth and Planetary Science Letters*, *226*(1–2), 225–241. https://doi.org/10.1016/j.epsl.2004.07.029

Tulk, C. A. (1999). Storage and handling of natural gas hydrate. *Bulletin of the Geological Survey of Canada*, (544).

Uchida, T., Dallimore, S., & Mikami, J. (2000). Occurrences of Natural Gas Hydrates beneath the Permafrost Zone in Mackenzie Delta: Visual and X-ray CT Imagery. *Annals of the New York Academy of Sciences*, *912*(1), 1021–1033. https://doi.org/10.1111/j.1749-6632.2000.tb06857.x

Waite, W. F., Winters, W. J., & Mason, D. H. (2004). Methane hydrate formation in partially water-satulated Ottawa sand. *American Mineralogist*, *89*(July), 1202–1207. https://doi.org/10.2138/am-2004-8-906

Waite, W. F., Santamarina, J. C., Cortes, D. D., Dugan, B., Espinoza, D. N., Germaine, J., … Yun, T.-S. (2009). Physical properties of hydrate-bearing sediments. *Reviews of Geophysics*, *47*(4), RG4003. https://doi.org/10.1029/2008RG000279

Yun, T. S., Francisca, F. M., Santamarina, J. C., & Ruppel, C. (2005). Compressional and shear wave velocities in uncemented sediment containing gas hydrate. *Geophysical Research Letters*, *32*(10), L10609. https://doi.org/10.1029/2005GL022607

Table 1. Values used in the HBES model runs (Marín-Moreno et al., 2017). Marín-Moreno et al. (2017)

Parameter	Value	Units	Reference
Hydrate bulk modulus	7.9×10^9	Pa	(Best et al., 2013)
Hydrate shear modulus	3.3×10^9	Pa	(Best et al., 2013)
Hydrate Poisson's ratio	0.32		
Methane bulk modulus	$K_{CH4}(P_p, T)$	Pa	(Millero et al., 1980)
Methane density	$\rho_{CH4}(P_p, T)$	kg m^{-3}	(Millero et al., 1980)
Methane viscosity	$\mu_{CH4}(P_p, T)$	Pa s	(Millero et al., 1980)
Methane irreducible saturation	0.02		(*Reagan and Moridis*, 2008)
Sand/Quartz grain bulk modulus	36×10^9	Pa	(Ecker et al., 2000)
Sand/Quartz grain shear modulus	45×10^9	Pa	(Ecker et al., 2000)
Sand/Quartz grain Poisson's ratio	0.062		
Sand/Quartz grain density	2650	kg m^{-3}	(Ecker et al., 2000)
Sand/Quartz grain diameter	1×10^{-4}	m	(Best et al., 2013)
Sand/Quartz grain coordination number	8.5		(Ecker et al., 2000)
Water bulk modulus	$K_W(P_p, T)$	Pa	(Setzmann & Wagner, 1991)
Water density	$\rho_W(P_p, T)$	kg m^{-3}	(Setzmann & Wagner, 1991)
Water viscosity	$\mu_W(P_p, T)$	Pa s	(Setzmann & Wagner, 1991)
Water irreducible saturation	0.2		(Reagan & Moridis, 2008)
Intrinsic permeability without hydrate	10^{-13}	m^2	(Daigle et al., 2015)
Intrinsic permeability exponent for cementing hydrate	3		
Intrinsic permeability exponent for pore-filling hydrate	2		
Tortuosity	3		based on (Mavko et al., 2009)
van Genuchten's (1980) capillary pressure fitting parameter	0.45		(Reagan & Moridis, 2008)
van Genuchten's (1980) capillary pressure gas entry parameter	2000	Pa	(Reagan & Moridis, 2008)
Critical porosity	0.36		(Mavko et al., 2009)
K Feldspar bulk modulus	37.5×10^9	Pa	(Mavko et al., 2009)
K Feldspar shear modulus	15×10^9	Pa	(Mavko et al., 2009)
Illite bulk modulus	62.21×10^9	Pa	(Mavko et al., 2009)
Illite shear modulus	25.70×10^9	Pa	(Mavko et al., 2009)

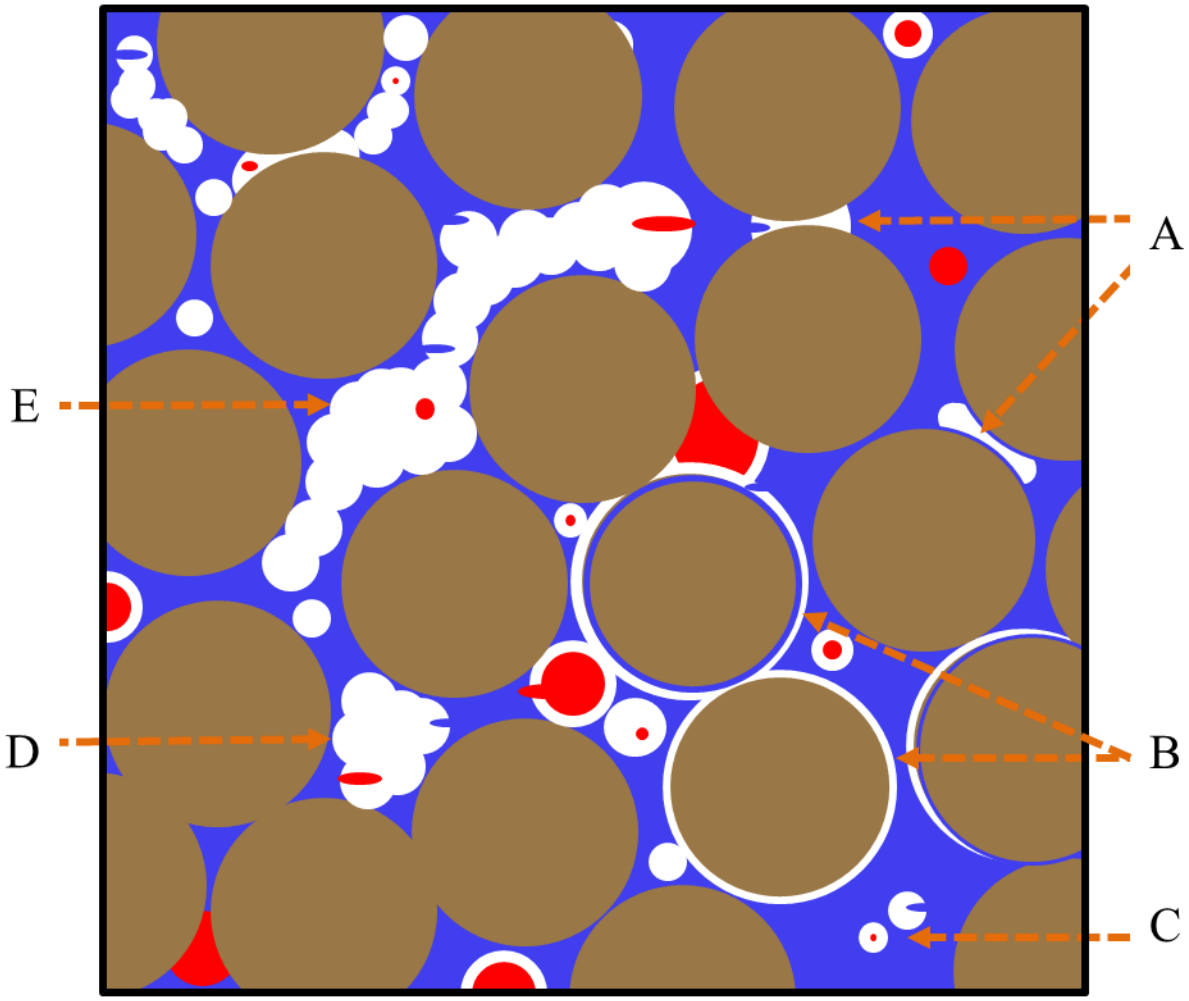

Figure 1. Conceptual diagram showing different pore-fluid displacing hydrate morphologies. A: Contact cement, B: Grain coating cement, C: Pore-floating, D: Pore-bridging and E: Inter-pore hydrate framework.

(a)

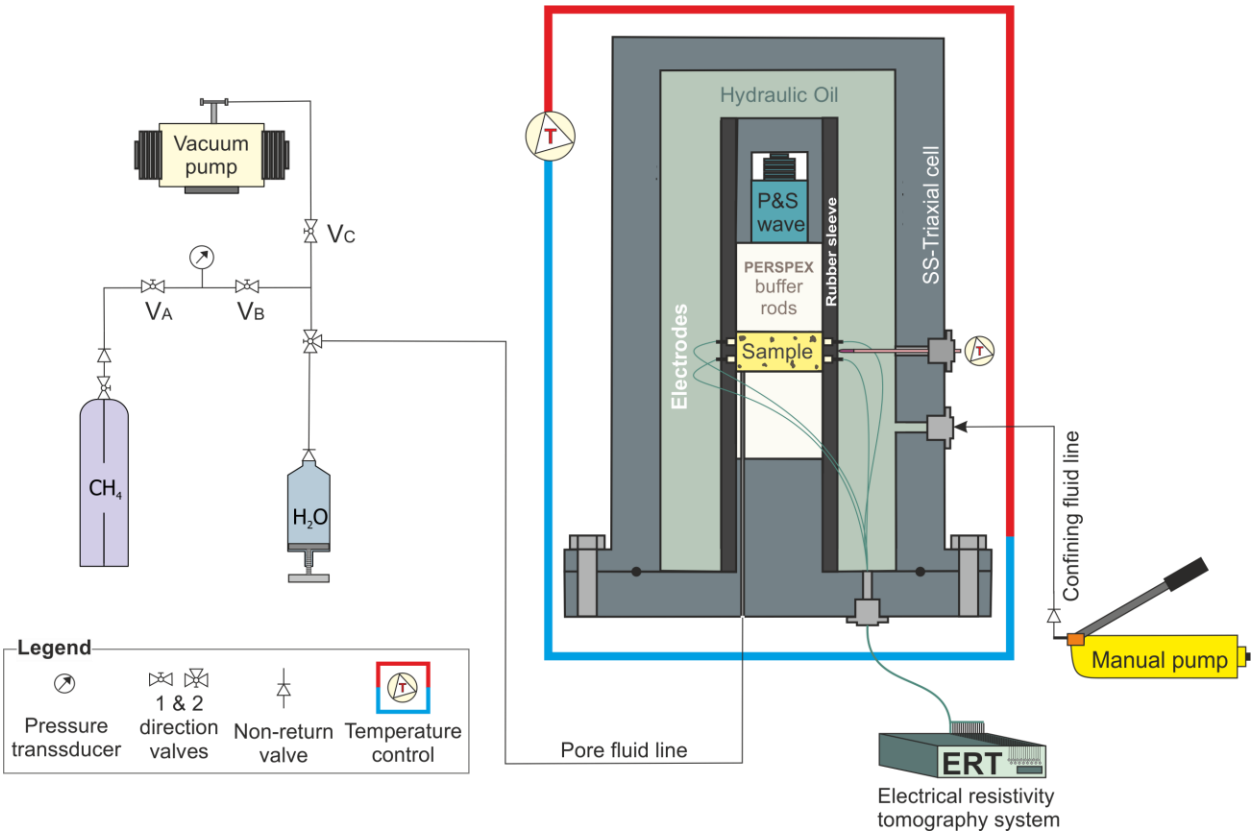

(b)

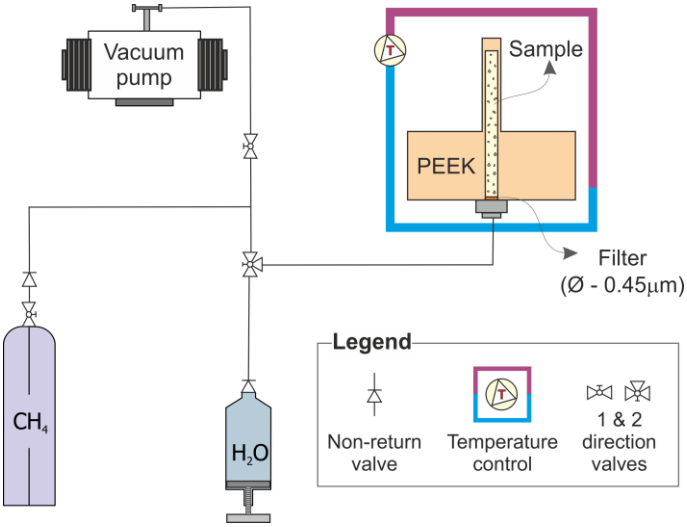

Figure 2. Schematic representation of the experimental setup: a) ultrasonic rig; b) synchrotron rig.

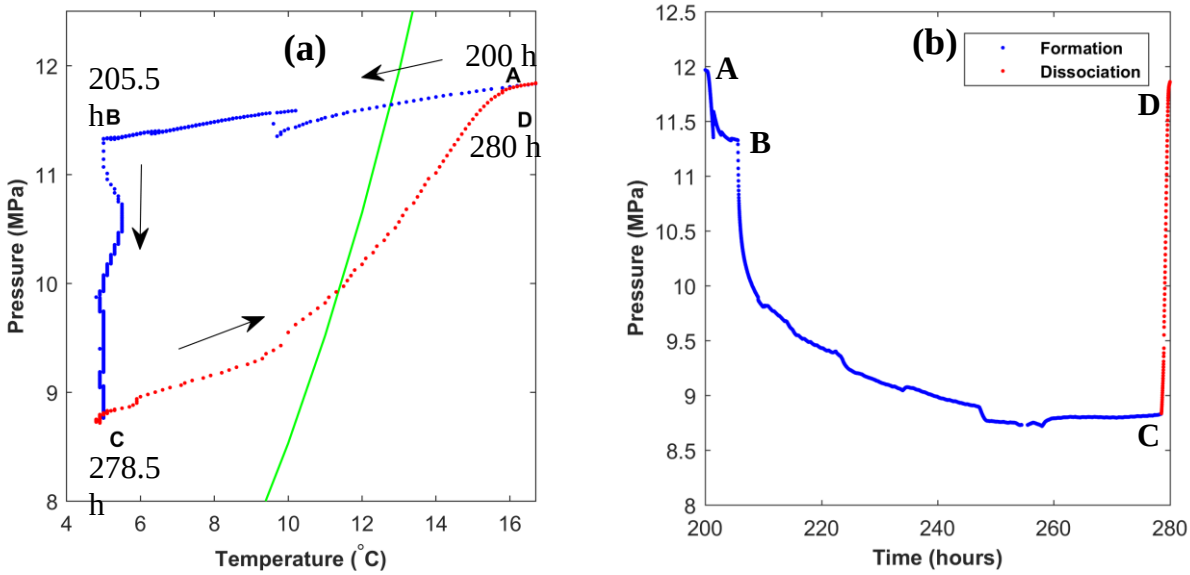

Figure 3. Changes of a) pressure and temperature and b) pressure with time during methane hydrate formation and dissociation in the Berea sandstone. Only the second cycle of hydrate formation and dissociation is shown for clarity. The green line is the methane hydrate phase boundary for 35 g/L salinity, calculated using the approach of Tohidi et al. (1995). Blue dots represent cooling and red dots represent heating. In a) time is shown in hours (h). Trajectory ABC marks cooling of the system to 5 ^{o}C and hydrate formation. Trajectory CD shows hydrate dissociation.

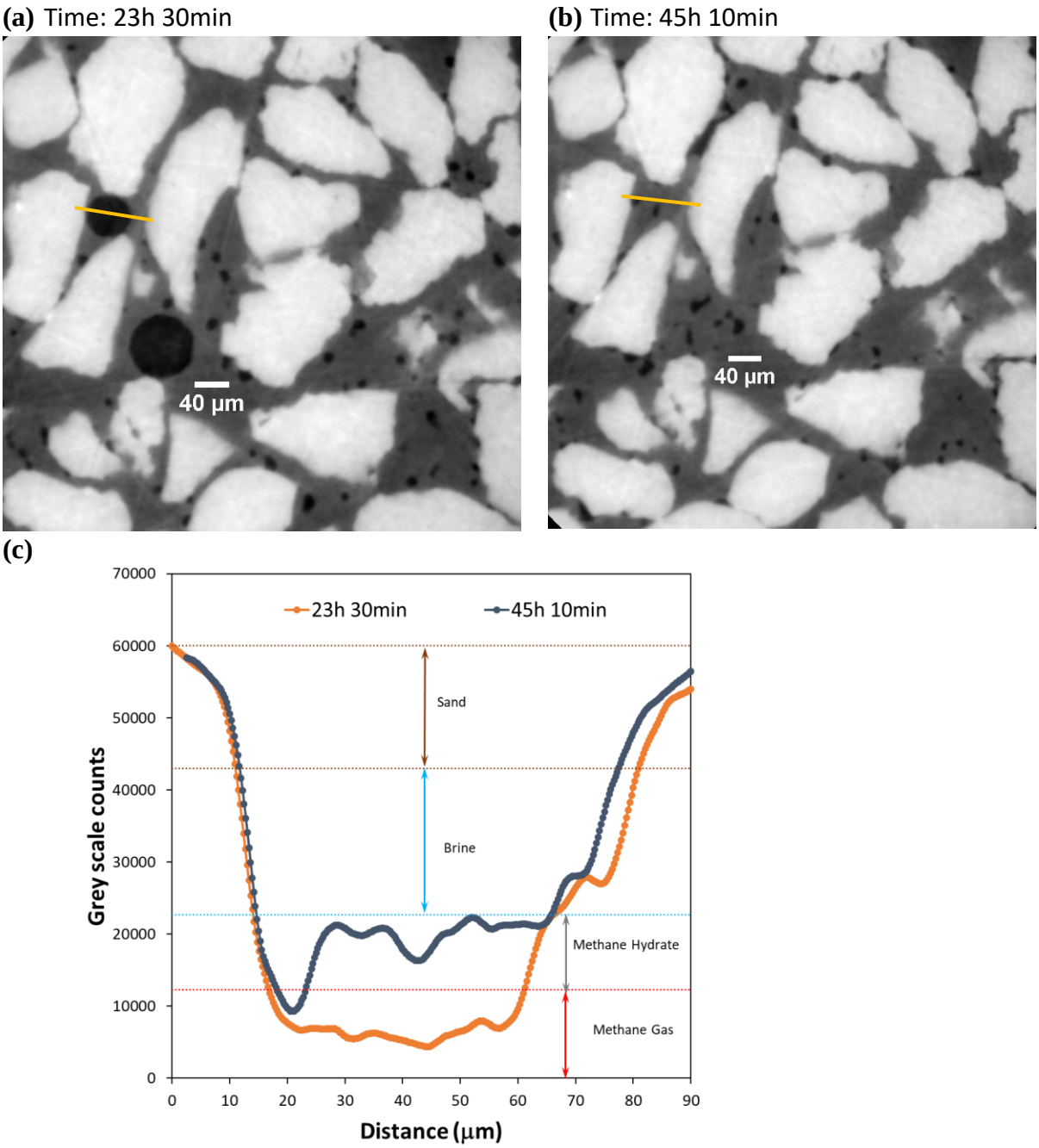

Figure 4. 2D phase reconstructed CT slices from synchrotron imaging of the hydrate/sand sample after (a) 23hr 30m, (b) 45hr 10m. (c) Cross section through grey scale images indicating evolution of hydrate formation extracted at the same locations shown in (a) and (b) marked in yellow. Also shown are the grey levels of the four phases methane gas, methane hydrate, brine and sand obtained by density normalization.

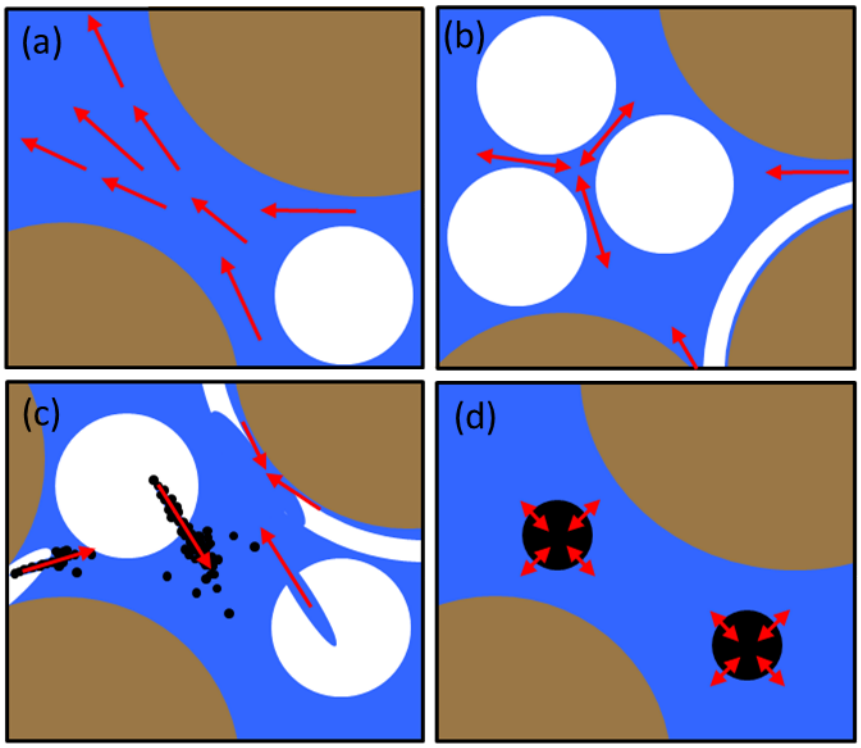

Figure 5. Conceptual diagram showing different loss mechanisms considered in the Hydrate-Bearing Effective Sediment (HBES) model of Marín-Moreno et al. (2017) a) Biot's type global fluid flow, b) micro squirt flow c) sub-micro squirt flow due to inclusions of gas and water in hydrates and d) gas bubble resonance. Blue represents water, black is gas and white is hydrate. After Marín-Moreno et al., (2017).

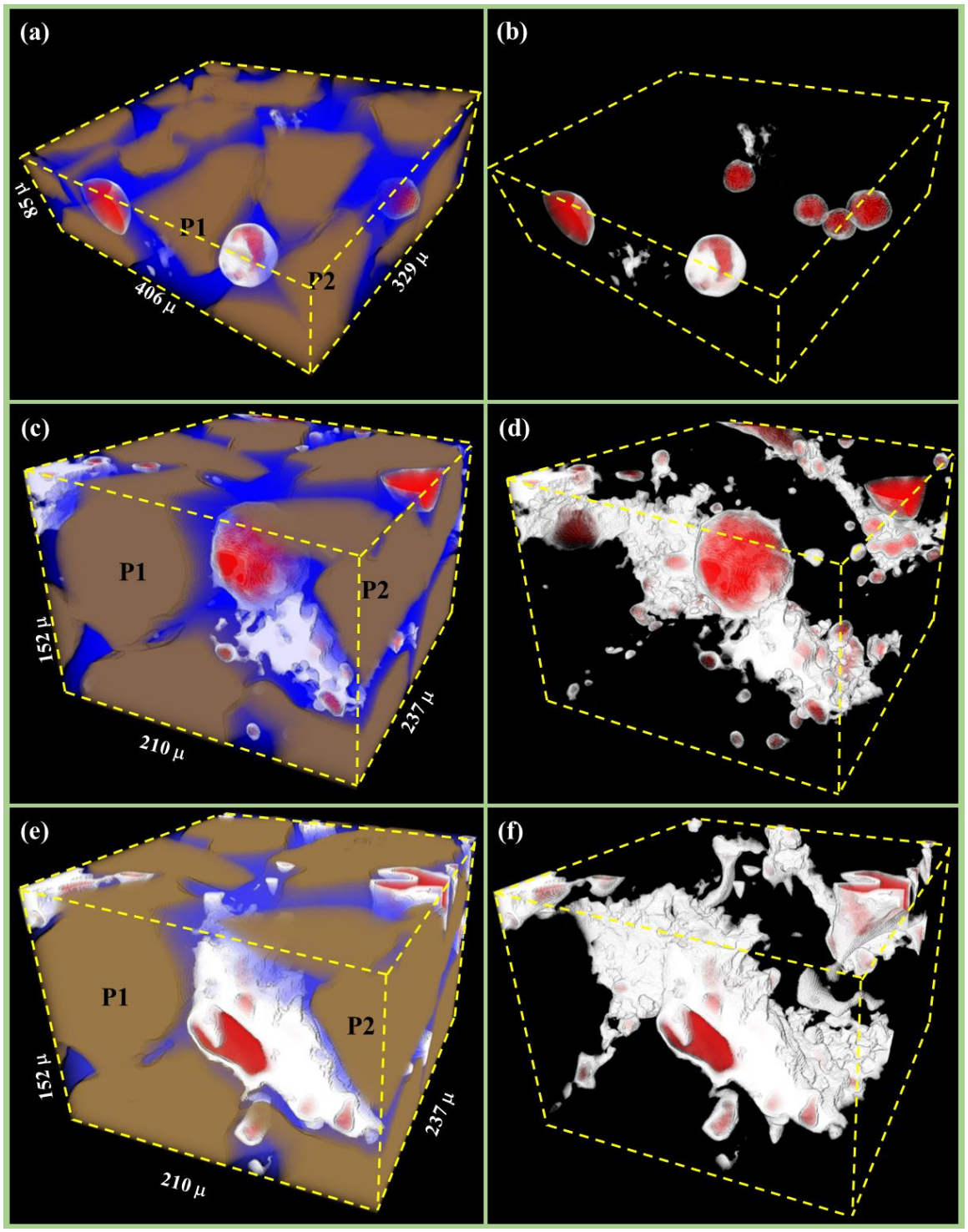

Figure 6. 3D Synchrotron radiation X-ray computed tomography images at different times during hydrate formation in sand. Red is gas, brown is sand, white is hydrate and blue is water. P1 and P2 marked in (a), (b) and (c) are two arbitrarily selected sand grains to aid visual comparison. Times are: 16hr 42 m (a and b), 23h 30m (c) and (d), 45h 10m (e) and (f). (a), (c) and (e) show all four phases while (b), (d) and (f) show only gas and hydrate for the same data volumes, respectively.

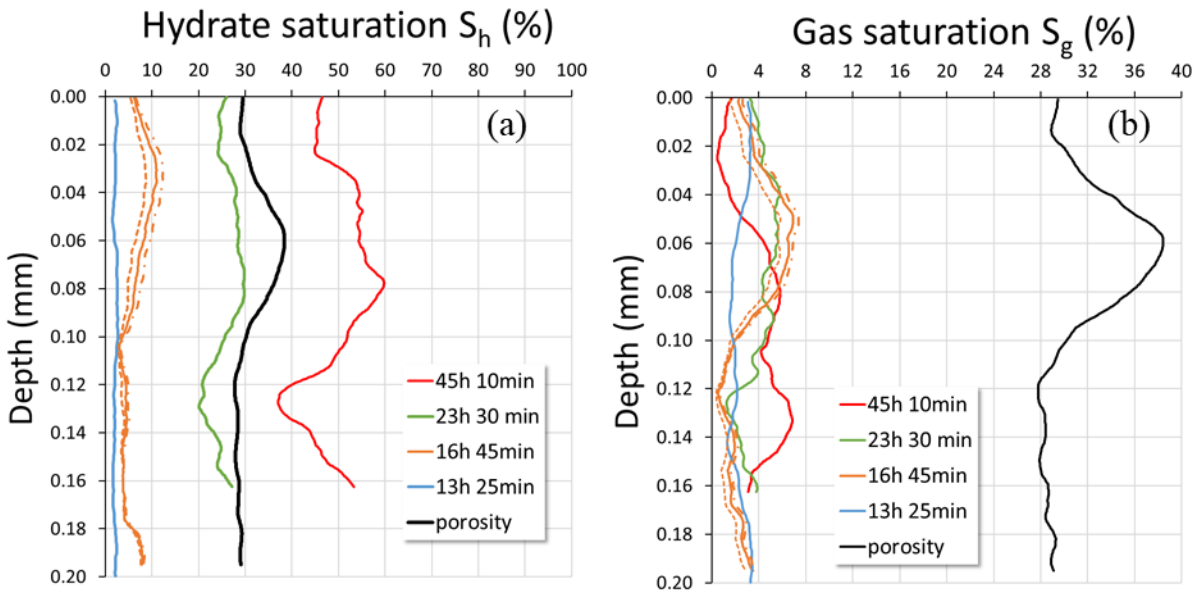

Figure 7. Changes in the samples' average areal distribution with depth of (a) hydrate and (b) gas at different times during hydrate formation in the X-ray CT analysis. Porosity distribution is also shown in (a) and (b). Dashed and dotted orange lines show the upper and lower error bounds for 16h 45m; errors bounds at other times are similar.

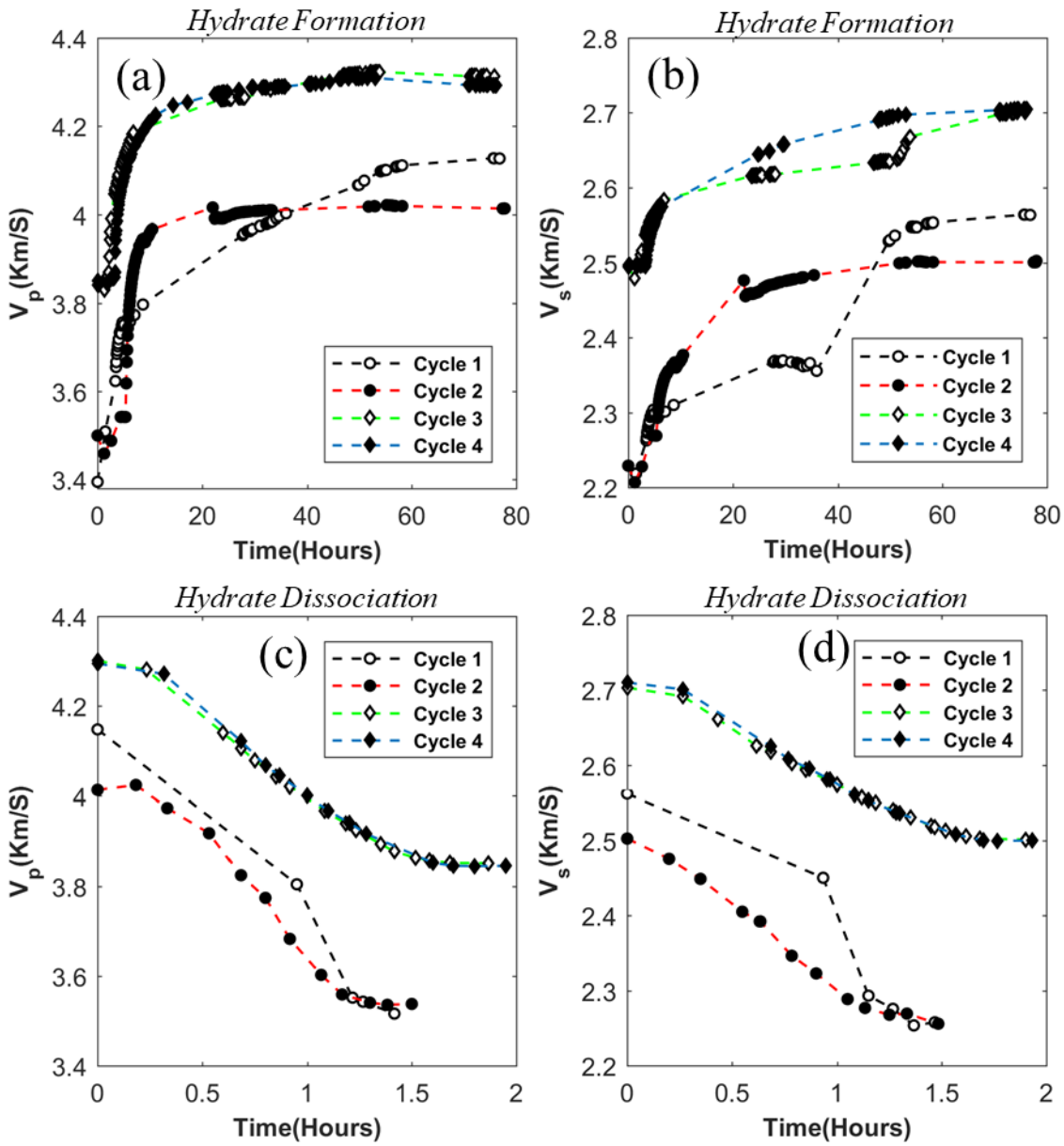

Figure 8. Changes in ultrasonic (648 kHz) P- and S-wave velocity (V_p, V_s) during hydrate formation (a, b) and dissociation (c, d). Differential pressure was 10 MPa for cycles 1 & 2, and 55 MPa for cycles 3 & 4. Although the cycles are continuous and sequential, zero time for a given cycle marks the beginning of cooling or heating for hydrate formation or dissociation, respectively.

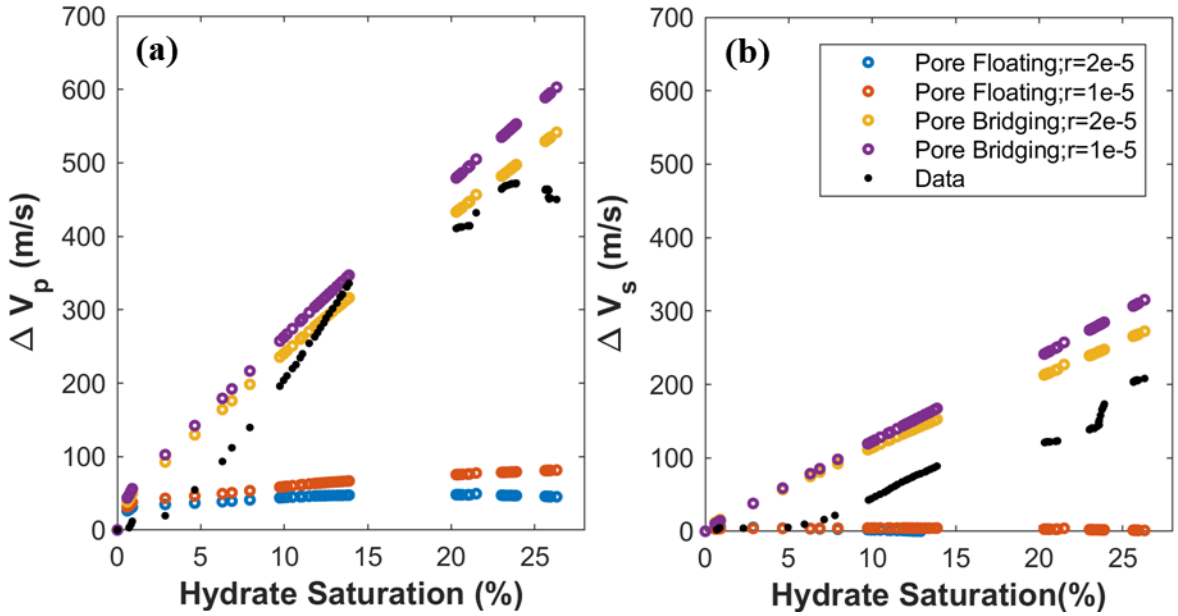

Figure 9. Comparison of measured and modeled change in (a) P- and (b) S-wave velocity with hydrate formation. The experimental data is that of the third cycle of hydrate formation with a differential pressure of 55MPa. The modeled velocities were obtained using the HBES model (Marín-Moreno et al., 2017) with two bubble radii of 2 x 10^{-5} m and 1 x 10^{-5} m. The error in the experimental data is smaller than the symbol size.

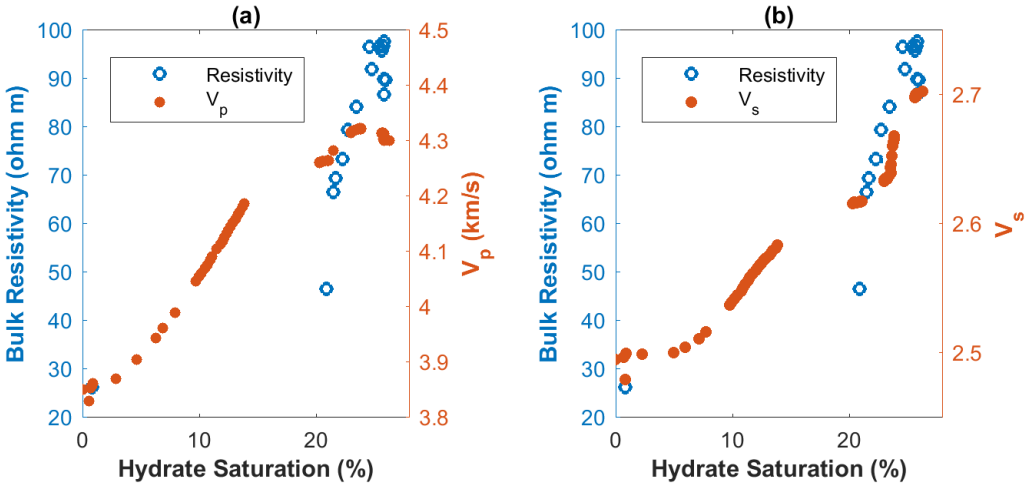

Figure 10. Changes in electrical resistivity and (a) P- and (b) S-wave velocity with hydrate saturation during cycle 3. The error in the experimental data is smaller than the symbol size.

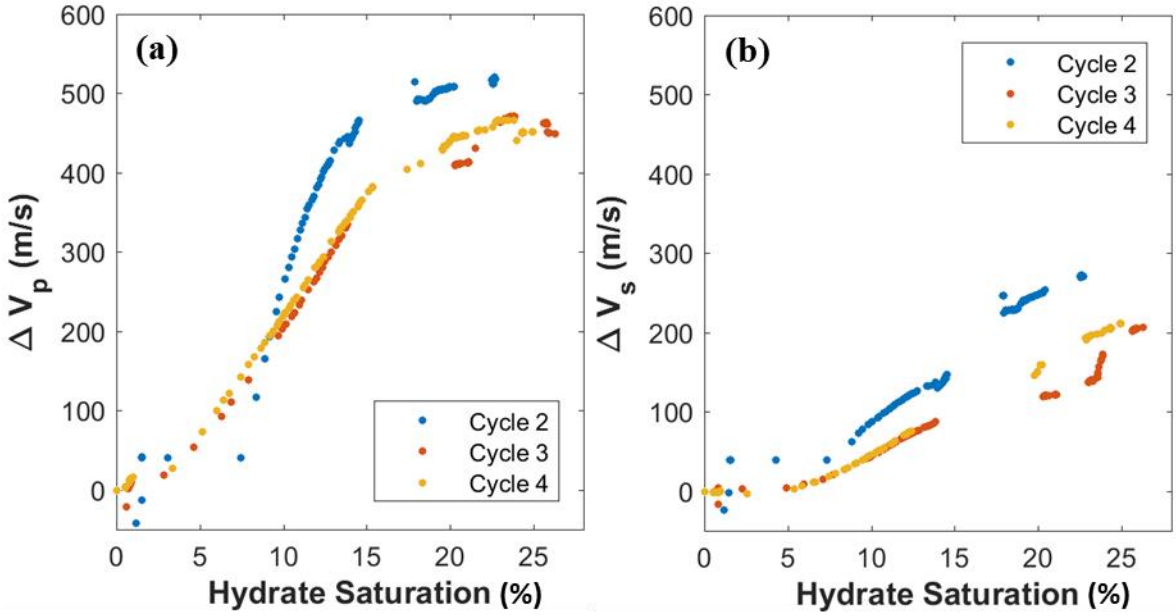

Figure 11. Changes in a) P- and b) S-wave velocity with hydrate saturation at differential pressures of 10 MPa (cycle 2) and 55 MPa (cycles 3 and 4). Saturations for cycle 1 are not shown because they could not be calculated due to a nonfunctional pressure gauge.